Magnetic connectivity in SEP events

Master's Thesis
University of Turku
Dept. of Physics and Astronomy
Physics
2019
BSc Suvi Barcewicz
Reviewed by:
Professor Rami Vainio
Adjunct professor Silja Pohjolainen

The originality of this thesis has been checked in accordance with the University of Turku quality assurance system using Turnitin OriginalityCheck service.

UNIVERSITY OF TURKU
Department of Physics and Astronomy
BARCEWICZ, SUVI Magnetic connectivity in SEP events
Master's Thesis, 52 pages, 1 appendix
Physics
October 2019
The originality of this thesis has been checked in accordance with the University of Turku quality assurance system using the Turnitin Originality Check service

---

The Solar energetic particle (SEP) events are the main source of the energetic particles we observe in space. They pose a threat on spacecraft electronics and humans in space and have effects that can be observed even from the ground, so studying these events is essential.

Energetic charged particles propagate mainly along the magnetic field in the interplanetary medium. In this thesis we look for a magnetic connection between the flare and the observer during the associated SEP event. The events studied here have Fe/C enhancement, indicating acceleration by a flare, but there is an associated coronal mass ejection (CME) as well. The magnetic connection was modeled by the angle between the root of the nominal Parker spiral and the potential field source surface (PFSS) modeled field line traced up from the flare site reaching closest to it.

More than ten open field lines were found within 10° from the flare site in 75% of the events. In 49% of these events we found a good magnetic connection. Good magnetic connection was associated with high Fe/C ratio, indicating flare acceleration and that the observed particles could have reached the observer from the flare. The flare parameters, duration and class, were not linked to the magnetic connection. The flare class, however, showed a connection to CME speed and the flare duration was associated with both, the CME speed and the Fe/C ratio of the SEP event.

We also studied the magnetic spreading of the PFSS model when tracing the field up from the flare site and found wider longitudinal spreading than in the previous studies. This explains how an SEP event can be observed by spacecraft almost on the opposite sides of the Sun.

Keywords; Sun, SEP event, flare, CME, magnetic field, magnetic spreading, magnetic connection, Fe/C

TURUN YLIOPISTO
Fysiikan ja tähtitieteen laitos
BARCEWICZ, SUVI Magneettinen yhteys Auringon hiukkaspurkausten aikana
Pro Gradu, 52 s., 4 liites.
Fysiikka
Lokakuu 2019

Auringon hiukkaspurkaukset tuottavat suurimman osan avaruudessa havaitsemistamme suurienergiaisista hiukkasista. Ne ovat haitallisia ihmisille ja elektroniikalle avaruudessa ja niiden vaikutus voidaan havaita myös maan pinnalla. Siksi niiden tutkiminen ja ennustaminen on tärkeää.

Varatut hiukkaset liikkuvat avaruudessa pääsääntöisesti magneettikenttää pitkin. Tässä pro gradu -tutkielmassa tarkastelen magneettista yhteyttä Auringon roihupurkausten ja havaitsijan välillä hiukkaspurkausten aikana. Tutkittavilla hiukkaspurkauksilla on kohonnut Fe/C-suhde, joka indikoi hiukkaskiihdytystä Auringon roihussa, vaikka tutkittaviin hiukkaspurkauksiin liittyi myös koronan massapurkaus (CME). Kuvasin koronan magneettikenttää potential field source surface (PFSS) -mallilla laskemalla kenttäviivat roihun lähistöltä lähdepinnalle. Magneettista yhteyttä kuvaa Parker-spiraalin kiinnityskohdan ja lähimmän kenttäviivan kulmaetäisyys lähdepinnalla.

Löysin PFSS-mallilla vähintään kymmenen avointa (lähdepinnalle ulottuvaa) kenttäviivaa 10° säteellä roihun koordinaateista 75% tapauksista. 49%:ssä näistä tapauksista löysin hyvän magneettisen yhteyden, eli löysin PFSS-mallinnetun kenttäviivan pään lähdepinnalta alle 10° päästä nominaalisen Parker-spiraalin juuresta. Hyvä magneettinen yhteys liittyi korkeaan Fe/C-suhteeseen, mikä viittaa siihen, että roihun kiihdyttämät hiukkaset voivat saavuttaa havaitsijan. Roihun kestolla ja intensiteetillä, ei ollut yhteyttä magneettiseen yhteyteen. Roihun intensiteetti oli sen sijaan yhteydessä CME:n nopeuteen ja roihun kesto sekä CME:n nopeuteen, että hiukkaspurkauksen Fe/C-suhteeseen.

Tutkin myös magneettikentän leviämistä PFSS-mallissa. Laskin kenttäviivat roihun läheltä ja mittasin suurimman longitudileveyden lähdepinnalla. Löysin suurempia leviämisiä, kuin aiemmissa tutkimuksissa, mikä selittää miksi kaksi havaitsijaa lähes vastakkaisilla puolilla Aurinkoa voivat havaita saman hiukkaspurkauksen.

Asiasanat: Aurinko, hiukkaspurkaus, roihu, koronan massapurkaus, magneettikenttä, magneettinen yhteys, Fe/C

Contents

List of abbreviations

CME	Coronal Mass Ejection
EIT	Extreme ultraviolet Imaging Telescope
EUV	Extreme ultraviolet
FIP	First ionization potential
GLE	Ground Level Enhancement
HEEQ	Heliocentric Earth Equatorial coordinate system
HMI	Helioseismic and Magnetic Imager
IMF	Interplanetary magnetic field
IPM	Interplanetary medium
MDI	Michelson Doppler Imager
PFSS	Potential Field Source Surface
POS	Plane-of-sky
SDO	Solar Dynamics Observatory
SEP	Solar Energetic Particle
SOHO	Solar and Heliospheric Observatory
SSW	SolarSoftWare

Introduction

The purpose of this thesis is to study the magnetic connection between a flare and observer during a solar energetic particle (SEP) event. The sources of these particles are solar flares and coronal mass ejections (CMEs), but the relative roles of these in the particle acceleration processes are still under debate. Therefore we will investigate if there is a magnetic connection between the flare and the observer, which would help us reveal if the flare site is an accelerating site for the particles.

The solar magnetic field has been observed indirectly for a long time by, e.g., counting sunspots and observing geomagnetic activity. Direct measurements of the solar magnetic field are available for four solar cycles. The heliospheric magnetic field is a dynamic system evolving periodically over time, the simplest heliospheric magnetic field configuration is dipolar, see on left in figure 1. Dipolar field is observed along with the sunspot number minimum, also known as the solar minimum, every 11 years. The maximum of sunspot number, or the solar maximum, is associated with a complex multipole field, as on the right in figure 1. [1]

The solar magnetic field observations agree well with Parker's [3] dynamo model. This model starts with a dipolar field, as on the left in figure 1. In the dense plasma below the solar surface the magnetic field is frozen into the plasma and as the ball of fluid undergoes differential rotation, the magnetic field turns from the poloidal

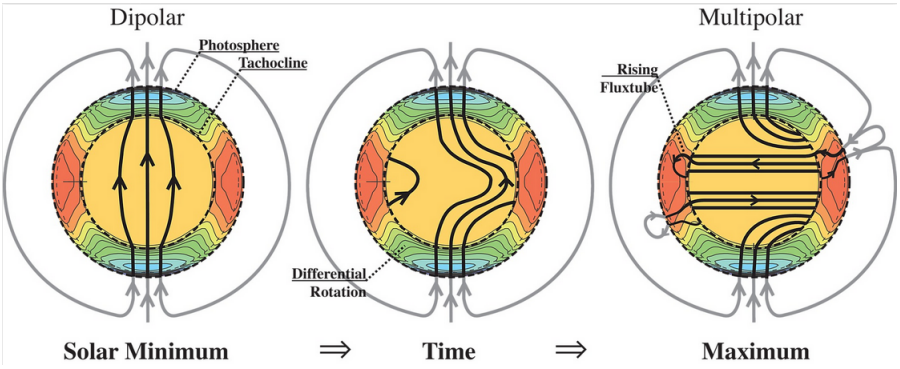

Figure 1. The development of the solar magnetic field from the solar minimum to maximum, as presented by Paul Higgins [2].

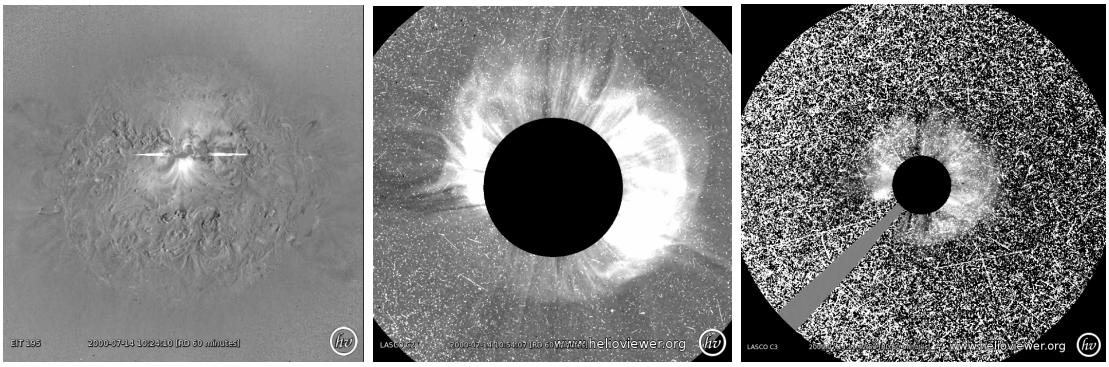

Figure 2. Pictures of the flare and the CME associated with SEP event on 14th of July 2000. All three are running difference images with a 60 minute interval. On the left SOHO/EIT 195 image at 10:19, the flare visible. In the middle SOHO/C2 image at 10:59, the CME clearly visible. On the right SOHO/C3 image at 11:59, visible the expanding CME and the solar energetic particles hitting the CCD of the coronagraph. Pictures produced from helioviewer.org.

to toroidal field. According to Parker [3] the rising magnetic flux tube, like in the picture on the right in figure 1, pushed by the coriolis force, appears above the photosphere as poloidal, but with opposite orientation to the original field. Eventually the whole dipole has turned around and a new cycle can begin.

The rising flux tube, such as on the right in figure 1, creates a pair of sunspots, a typical environment for a flare or a CME. Reames [4] writes, "Magnetic energy released from the reconnection of these [tangled coronal magnetic] fields probably powers flares and triggers the release of CMEs." In a flare the energy and the particles are held in magnetic loops, resulting in hot plasma which cools by emitting radiation. In a CME the energy appears as the kinetic energy of the magnetic cloud.

A solar flare was first observed in 1859 by Carrington [5]. Only the strongest flares can be observed in white light, as Carrington did. Line emission is more typically associated with flares, for example the Hα line. Flares can, however, emit radiation over the whole electromagnetic spectrum from X-rays to radio. Flare observation by Extreme ultraviolet Imaging Telescope (EIT) on board Solar and Heliospheric Observatory (SOHO) on the left in figure 2. EIT 195, refers to EIT

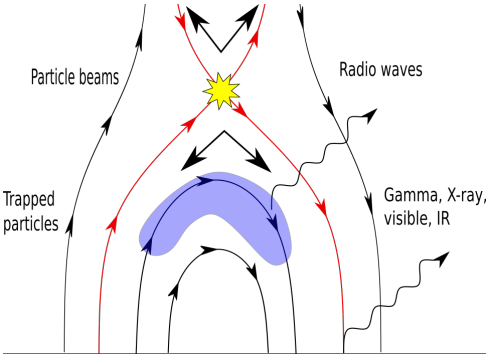

Figure 3. Schematic of the particle populations and electromagnetic emissions during a flare adapted from [6].

observations at 195 Å, which corresponds to Fe XII spectral line.

In figure 3 there is a cartoon showing the different emitting sources of the flare. The energy release above the loop top happens by magnetic reconnection, yellow star in figure 3, it accelerates particles up along the open field lines (they might also be a part of another closed structure), and down back towards the solar surface. Trapped particles in the magnetic loop emit thermal X-ray and radio waves and the fast particles that end up reaching the solar surface causing emission in hard X-ray (bremsstrahlung by electrons), gamma (nuclear line excitation caused by protons), visible and infrared wavelengths.

According to Chen [7] the credit for finding the CMEs goes to Richard Tousey [8] who studied OSO-7 (Orbiting Solar Observatory 7) coronagraph observations from 1971 December 14 and found plasma clouds moving through the corona. He published his results in 1973, over 100 years after the discovery of solar flares. CMEs are often associated with flares, but they occur also separately. They are thought to be different symptoms of the same magnetic "disease". Coronagraph observations of a CME are in the middle and on the right in figure 2. These images are from Large Angle and Spectrometric Coronagraph (LASCO) on board SOHO, C2 shows the corona from $1.5\,R_\odot$, $R_\odot$ denoting solar radius, to $6\,R_\odot$ and C3 shows the corona from $3.7\,R_\odot$ to $30\,R_\odot$. CMEs are also normally accompanied by shock related phenomena,

i.e., type II radio bursts, Moreton waves, and EIT waves. More details about CMEs can be found, e.g., from the review by Chen [7].

Both flares and CMEs, are associated with SEPs, which are increases in the energetic particle flux observed in the interplanetary medium (IPM). This is an important topic in space research as the SEPs are a huge threat to spacecraft electronics as well as humans in the space. Prediction of SEP events and space weather is thoroughly discussed, e.g., by Klein & Dalla [6] and Malandraki & Crosby [9].

In this thesis we study the magnetic connection of solar flares with Earth to find out more about the particle acceleration mechanisms. In chapters 1 and 2 we introduce the background, the SEPs and the heliospheric and coronal magnetic field. In chapters 3 and 4 we present the data and our results and finally in chapters 5 and 6 offer our conclusions and some outlook.

1 Solar energetic particle events

The first SEPs were observed in the 1940s by Forbush [10] in ground-level ion chambers as a sudden rise in the cosmic ray intensity. Nowadays these are called ground level enhancements (GLEs). They occur when GeV protons cause a nuclear cascade in the Earth's atmosphere. In the forties CMEs were still to be found, so Forbush [10] suggested that the particles were accelerated by a changing magnetic field of sunspots that were located near the observed flare. For a long time the properties of SEP events were explained considering transport from a point source rather than by the acceleration mechanisms or the spatial characteristics of the source itself.

In 1963 Wild et al. [11] described radio observations and their relationship with other phenomena. They describe two phases of the flare: First a fast explosive event accelerating electrons into $\sim 100\,\mathrm{keV}$ energies, which can be observed as a type III radio burst. Second phase occurs with large flares, it appears as a type II radio burst, which can be interpreted as a disturbance traveling out of the Sun at a speed

higher than the local sound speed, probably a magneto-hydrodynamic shock wave, which can accelerate both protons and electrons into very high energies ($\sim$ GeV, [12]). This shock wave was later found to be driven by a CME.

In 1986 Cane et al. [13] found different proton and electron abundances in SEP events associated with short and long duration X-ray events and so the SEP events were divided into impulsive and gradual. Such X-ray time scale does not describe the different acceleration processes involved, but similar difference is visible in the length of the SEP event as well. A wider review on the history of SEPs is given by, e.g., Reames [4].

1.1 Gradual SEP events

Gradual SEP events are large, most intensive, and have longest durations of the SEP events. About twenty gradual SEP events are observed each year around solar maximum. [4]

1.1.1 Related phenomena

Gradual SEP events are associated with fast CMEs and type II radio bursts, which indicate a shock wave propagating through the corona. Reames et. al. [14] found that CMEs with a speed $> 750\,\mathrm{km\,s^{-1}}$ produce an SEP event, but CMEs with a speed $< 500\,\mathrm{km\,s^{-1}}$ do not. The CME must be significantly faster than the ambient solar wind to drive a shock that can accelerate coronal particles.

Gopalswamy et al. [15] studied the type II radio bursts and CMEs and found a large variation in the local Alfvén speed in the corona, which indicates that CME speed alone does not tell about the shock-driving capability of the CME, but the conditions of the ambient medium play an important role as well. Even CMEs as fast as $1000\,\mathrm{km\,s^{-1}}$ do not always drive a shock. A better measure for the shock strength would be the Mach number, finding the Mach number is rather tedious compared

to considering the plane-of-sky (POS) speed of the CME, but can be done, see the work of, e.g., Afanasiev et al. [16]. On the other hand the POS speed of the CME is kind of a minimum estimate of the full vector. Kouloumvakos et al. [17] found the strongest correlation between the shock Mach numbers and SEP peak intensities while studying the properties of CMEs and associated SEP events.

Figure 3 shows a possible magnetic topology below the CME, when a large CME is associated with a flare. In this case the particles accelerated by the flare stay in the closed loops below the reconnection site or above it in the magnetic cloud driving the CME. This is similar to the topology presented by Reames [18], in both pictures the particles can not escape along open field lines, but must travel along with the magnetic cloud.

1.1.2 Acceleration mechanism

Gradual events are large, intense and spatially widely distributed, they are gradual because continuous acceleration of particles provides a broad long-lasting source of particles in the inner heliosphere.

Particle acceleration in a shock happens as particles cross the shock between the upstream and downstream regions multiple times. Multiple crossings can be caused either by scattering off turbulent magnetic fluctuations, (e.g., [19]) or in the absence of turbulence, by large scale magnetic-field inhomogeneities around the shock [20].

This picture of pure shock acceleration is contrasted by Marque [21], who found only a few events with a fast CME or filament eruption with no evidence of an associated flare, and these events did not produce an SEP event. Their conclusion was that either CMEs do not accelerate particles on such wide fronts as we believe or the shocks are not very effective in accelerating particles above $\sim 10\,\mathrm{MeV}$ energies. Maybe the role of CMEs in SEP events lies instead or in addition to acceleration in creating magnetic connection to the heliosphere.

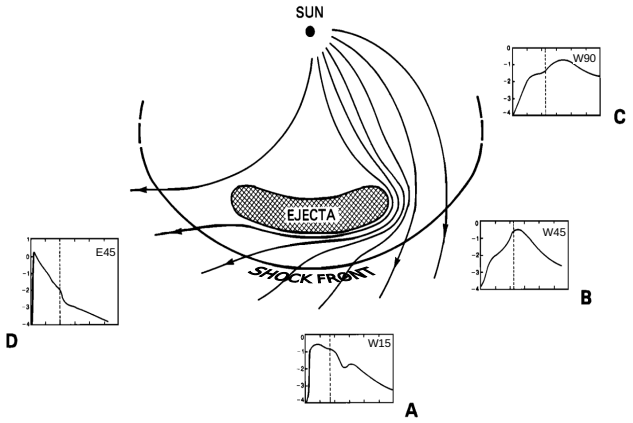

Figure 4. The shape of the time-intensity profile differs widely depending on which part of the CME front the observer is magnetically connected to. Dashed vertical line indicates the shock crossing. Figure adapted from [22].

1.1.3 Time-intensity profile

Intensity-time profiles of gradual SEP events are wide, events can last for days. There are, however, many shapes of the profiles depending often on the location of the observer with respect to the trajectory of the CME, see figure 4. As described by Reames [12], observers located East from the CME trajectory normally see the SEP intensities peak early before the shock passage as they are best connected to the nose of the shock when it is still down in the corona. The shock is strongest in the direction of the propagation, nose of the shock, as on the flanks the velocity rises from expansion of the magnetic cloud, instead of the combination of the propagation and the expansion. Observers located near the path of the CME often see the highest intensities around the time of the shock passage as the magnetic connection with the shock front appears only as the CME approaches the observer. Observers located West from the CME trajectory see the intensities peak after the shock passage as they become magnetically connected with the shock nose only then, from behind (down stream side of) the shock. Observers on the trajectory or East from it would

see a sharp rise in the intensities as they become quickly connected with the nose of the shock as opposed to observers from the West side, who will see a slow rise as the field lines are first connected to the weak flanks of the shock and then slowly connection moves towards the effectively accelerating nose of the shock.

1.1.4 Abundances

The observed particle abundances in gradual events match the particle populations expected to be seen in corona, which is in agreement with the assumed CME-driven shock acceleration. Nowadays we normally use an average abundance from gradual SEP events as a reference when studying coronal, photospheric or impulsive SEP event abundances. Dividing the averaged abundances of gradual events by corresponding photospheric values shows a $\sim$ 3 fold difference between high and low first ionization potential (FIP). This difference arises as the high-FIP elements stay neutral in photosphere whereas the low-FIP elements ionize and the ions are more effectively transported to the solar corona by Alfvén waves for example. The charge state of iron in gradual events has been found to be 14.1 ± 0.2, which corresponds to $T \approx 2\,\mathrm{MK}$, in agreement with typical coronal temperature. The SEP particle abundances are thoroughly discussed by, e.g., Reames [12, 23].

1.2 Impulsive SEP events

Impulsive SEP events are small, weak and compact, but common where ever there is open field lines involved in reconnection. Occurence rate of impulsive SEP events is ~ 100 observed events per year near solar maximum. [4]

1.2.1 Related phenomena

Impulsive SEP events are associated with an impulsive flare, which sometimes comes with a narrow CME [24], and sometimes with an extreme ultraviolet (EUV) jet [25].

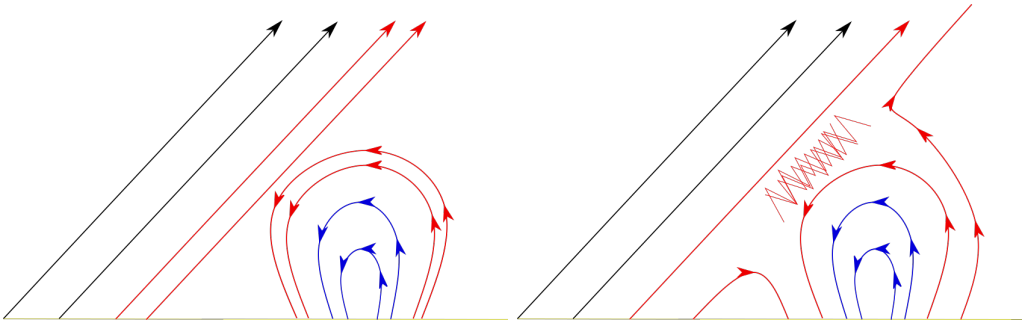

Figure 5. Schematic of the magnetic topology where reconnection involves open field lines and a flare can produce SEP particles. Open field lines are in black, closed ones in blue and red ones are taking a part in the reconnection. As the loop rises the opposite fields get pushed together and eventually create a current sheet where reconnection (marked with red) will rearrange the field lines. Figure adapted from [18].

The flares are observed by the thermal emission of the hot plasma, or the hard X-ray and type III radio bursts caused by the non-thermal electrons. Despite the special isotopic composition of these events nothing special was to be found about the flares, so impulsive SEP-events could be produced by any flares [4].

Jets are typically observed in EUV or soft X-rays near the photosphere and the reconnection site, as particles travel along the open field lines towards the upper right corner in the figure 5. Sometimes, however, enough plasma is being ejected that it can be seen in white-light coronagraph observations as well. [24]

1.2.2 Acceleration mechanism

There must be open field lines included in the magnetic reconnection to allow the flare to produce an SEP event, The magnetic topologies leading to two classes of SEP events are well described by Reames [18]. In figure 5 is a schematic of the magnetic topology of a flare, where open field lines are involved in reconnection. It is also possible that a blob of plasma gets ejected up and to the right in the image along the open field lines, this can be then observed as the narrow CME or a jet associated with the impulsive SEP events.

Magnetic reconnection is a process where the magnetic energy is transformed

into other energy forms, like heat and kinetic energy. In figure 3 the reconnection region is marked with a yellow star between two (red) magnetic field lines of opposite polarity. Another magnetic topology involving reconnection is presented in figure 5. The most basic and well known reconnection model is the Sweet-Parker model [26]. In this model two magnetic flux systems with different polarities are pushed together, creating a current sheet over the region with changing magnetic field. In this simplest form we assume a region where electromagnetic energy is flowing in and transforming into kinetic energy of the particles flowing in vertical direction in the figures 3 and 5.

Petrosian [27] gives a thorough review on solar flares and stochastic acceleration, emphasizing the importance of turbulence. In this view the reconnection changes the magnetic energy into turbulence, in figure 3 the blue loop top area is highly turbulent and hence a great environment for stochastic acceleration. Stochastic acceleration is a generalization of Fermi's idea that charged particles are accelerated by encountering magnetic obstacles, as energy is gained in head-on collisions which in the presence of a magnetic obstacle happen more often than trailing collisions. Such magnetic obstacle can be replaced by a fluctuating electric filed or turbulent plasma flow.

1.2.3 Time-intensity profile

Impulsive events are often small, not as intensive as the large gradual events. They are also short, the time a flare is accelerating particles is rather minutes or hours than days. The source itself is compact, so its size does not effect the time-intensity profile.

1.2.4 Abundances

The abundances are normally scaled to the average values of gradual SEP events. In the case of impulsive SEP events these scaled values show enhancements in heavy elements like Fe, but also ^{3}He.

Ionization state of iron in the impulsive SEP events is 20.5 ± 1.2. This is much higher than the ionization state observed during a gradual SEP event. Common explanations are that the plasma in the flare is hot and hence highly ionized or the ionization has taken place through impact ionization in dense plasma while particles are still trapped or during transport. [23]

Heavy element enhancements can be explained by their cyclotron frequency, which is directly proportional to their Q/A ratio [6]. As the frequency of the turbulent plasma waves grow, it can be expected to first resonate with ions with low cyclotron frequencies, i.e., ions with lower Q/A ratio. Hence these particles are expected to be more efficiently accelerated than species with higher Q/A ratio and cyclotron frequency. The Q/A ratio dependence of the enhancements fits the observations as presented by Reames [4]. This, however, does not explain the enhancement in ^{3}He.

Petrosian [27], as mentioned before, discusses the stochastic acceleration by turbulence and shows that when the effects of fully ionized ^{4}He are included in the dispersion relation ^{3}He ions are more likely to be accelerated in wave-particle interactions in turbulent regions than ^{4}He.

1.3 Hybrid SEP events

Dierckxsens et al. [28] studied SEP probability as a function of flare and CME properties. They found better correlation between proton peak flux at lower energy channels with the CME properties and at higher energy channels with the flare properties. Correlation with flare and CME properties was equally good in the

$15.12 - 21.87\,\mathrm{MeV}$ channel. This indicates hybrid events where both acceleration mechanisms take place. This would be in a good agreement with aforementioned result by Marqué et al. [21], that shocks might not be very effective in accelerating particles above $\sim 10\,\mathrm{MeV}$ energies.

Also Papaioannou et al. [29] studied a large sample of events and found it difficult to separate them into two classes. They did not, however, want to consider all of them hybrids either.

Tylka et al. [30] studied a set of hybrid events and found that enhancements in Fe/O could be explained by a suprathermal seed particle population from a previous flare, which is accelerated more efficiently by a quasi-perpendicular shock than the solar-wind plasma. This would be another way to explain these hybrid events, aside from there being a magnetic connection to the flare site, which we will be looking for in this thesis.

Petrosian [27] comes to a conclusion that the basic acceleration happens at the flare site and is common to all events. The spectrum produced by the flare can be further modified by a CME driven shock. Considering this scenario we get a whole spectrum of events with different properties, from impulsive events with no CME to events with insignificant acceleration (or the lack of) flare site.

As there is no consensus on the source of the SEP events it will be interesting to study how a carefully modeled magnetic connection behaves with respect to the parameters of the SEP event, CME and flare.

2 Coronal and heliospheric magnetic field

There is currently no routinely utilized reliable way to observe the magnetic field in the dilute plasma of the solar corona or the heliosphere, except for the in-situ measurements. The photospheric magnetic field instead can be observed by Zeeman splitting: the splitting of atomic spectral lines. If the magnetic field is along the

line of sight the observer can see the line split in two σ components, one on each side of the original line (λ_0), each with opposite circular polarization. If the field is perpendicular to the line of sight there will be two σ components as described before, but linearly polarized along the magnetic field and additionally in the place of the original line a π component with linear polarization perpendicular to the magnetic field. Even in strong magnetic fields observing these shifts is challenging as they are at optical wavelengths of the order of $\Delta\lambda/\lambda_0 \approx 10^{-6}$. This observation method limits our direct observations of the solar magnetic field to the photosphere, as we can not see through it and above it the corona is not dense enough to emit enough light to be observed by this method. [31]

2.1 PFSS model

In 1969 Altschuler et al. [32] introduced a potential field source surface (PFSS) model for the magnetic field in the solar corona. It has two basic assumptions: first, as our measurements of the magnetic field in the photosphere can not describe the electric currents in the corona, it is assumed to be current-free. The current-free approximation becomes very unrealistic around $2.6\,\mathrm{R}_\odot$ due to solar wind, so they thought that at a certain height (turns out $2.5\,\mathrm{R}_\odot$ fits the observations best) the magnetic field must turn into radial direction. This spherical surface is referred to as the source surface. Back in the sixties there was only Earth bound magnetograph data available, so the second assumption was that the changes in the photospheric magnetic field during one solar rotation do not effect the large scale magnetic field.

2.1.1 SolarSoftWare

The method described by Altschuler et al. [32] has been further developed by Schrijver et al. [33] to create a PFSS package for SolarSoftWare (SSW). SSW is a software library, which aims to provide an environment for solar physics data

analysis. There is a GUI interface for plotting simple pictures of the magnetic field, but through the command line interface SSW offers an opportunity to produce all different kinds of plots.

The PFSS package uses as a boundary condition a map of photospheric magnetic field that is based on measurements from Michelson Doppler Imager (MDI) on board SOHO or later The Helioseismic and Magnetic Imager (HMI) on board Solar Dynamics Observatory (SDO). Calibration from SOHO/MDI data to SDO/HMI data is well described by Liu et al. [34]. Because the method was originally developed for data from SOHO/MDI they use only the line-of-sight data from the both magnetograms. They do "correcting for line-of-sight effects by assuming the field to be vertical to the solar surface" Schrijver et al. [33]. As measurements on the Zeeman splitting can be done only near the central meridian and hence only once per soalr rotation, also the far-side acoustic information was included in the mapping of the photospheric magnetic field since 3rd September 2000. This gives information on appearing or dissappearing active regions behind the Sun. The details of these maps of the photosperic magnetic field are given by Schrijver et al. [33].

Schrijver et al. [33] describe also the mathematics of extrapolating the magnetic field from the solar surface to the source surface. Boundary conditions of the solution being the map of the radial magnetic field component on the solar surface, updated every 6 hours, and magnetic field being radial on the source surface.

One of the features of the method used in the PFSS package is that strong compact sources are best found by tracing the field from the source surface down to the solar surface whereas weak extended sources are best found by tracing the field up from the solar surface to the source surface. [33]

2.2 Connectivity

In his paper from 1958 Parker [35] introduces a spiral structure for the interplanetary magnetic field (IMF). The shape of each field line depends on the solar wind speed and the latitude. In this model the root points of the magnetic field are frozen into the solar surface and radial at the root. They bend into a spiral as the Sun turns around its axis, but the radial solar wind the magnetic field is frozen into supports the field lines from winding up to a tight ball. In figure 6 Parker spiral is sketched as blue curves. This image describes the shape of the field lines as they look on the solar equator, towards the poles the field lines become radial.

In 1942 Alfvén [36] introduced the Alfvén wave, which ties together the plasma movement and the magnetic field. This is an important basis for the particle transport in space, the frozen-in condition follows from this connection. Nowadays most particle transport models are in 1D, there is only the distance along the nominal Parker spiral as the particles with speeds far exceeding the solar wind speed are expected to follow along the magnetic field line. Despite this connection we can, however, observe SEP events with an associated flare far away from the foot of the nominal Parker spiral. The source longitudes span from E90 to W90, as described, e.g., by Klein & Dalla [6].

Term *connectivity* λ, in figure 6, in this thesis is used to describe the angular distance between the nominal Parker spiral foot point on the source surface and the source surface end of the closest PFSS modeled field line. The other connectivity used in this thesis is marked as β in figure 6, angular distance between the flare site and the closest PFSS modeled field line when the field lines a traced down from the source surface. The smaller the angle, the better the connection.

Similar studies of the connectivity have been done before on impulsive ^{3}He rich events. Nitta et al. [37] studied impulsive events and their identified source regions, they measured longitudinal distance between the source site and the PFSS field line

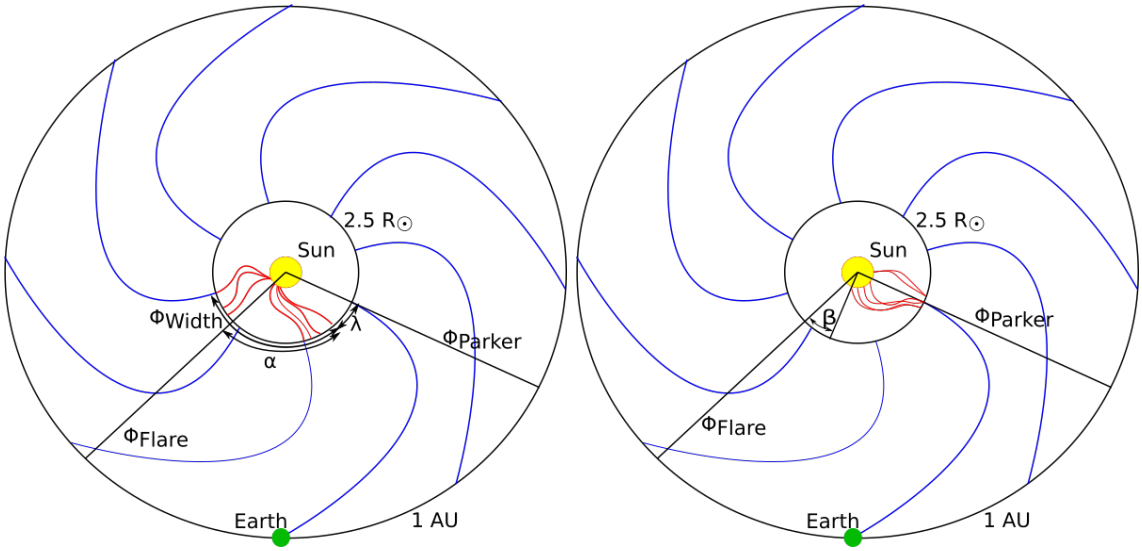

Figure 6. Heliospheric magnetic field. Inner circle with red magnetic field lines represent the PFSS model, blue field lines in the outer circle represent the Parker spiral. On the left PFSS field lines were traced up from the flare site, λ stands for connectivity, α is the largest angular distance between the flare site and a field line end point on source surface, Φ_{width} is the longitudinal width. On the right PFSS field lines were traced down from the source surface near the nominal Parker spiral and β describes the connectivity.

on the solar surface and the longitudinal distance between the nominal Parker spiral and the PFSS field line on the source surface and found the sum to be $< 10°$ in 40% of the events. Wang et al. [25] traced field lines ending up on source surface in the longitude range [W35, W65] and latitude range $[\Theta_{\text{Earth}} - 20°,\ \Theta_{\text{Earth}} + 20°]$. They found the angular separation between the source site and the closest PFSS field line to be 4°. All their sources were located on the western hemisphere, which makes finding such good connection likely.

3 Data analysis

3.1 Data

We will study SEP events listed in a paper by Raukunen et al. [38]. This data set was collected with Energetic and Relativistic Nuclei and Electron (ERNE), Torsti

et al. [39], instrument onboard the Solar and Heliospheric Observatory (SOHO) during the 23rd and 24th solar cycle, between years 1997 and 2015. These data were measured with Low Energy Detector (LED) and is therefore in the energy range $1 - 15\,\mathrm{MeV\,n^{-1}}$. These events are iron rich and the average CME velocity is $1090\,\mathrm{km\,s^{-1}}$, which is fairly low, e.g., Papaioannou et al. [29] found the average speed of SEP related CMEs to be $1390\,\mathrm{km\,s^{-1}}$, their sample was 158 events from 1984 to 2013. This list is, however, not a list of clearly impulsive events, there are fast, wide CMEs involved, and not all the Fe/C ratios are very high, although they are still all above coronal values. Our data set consists of observations on the SEP event, flare and CME. We dropped out events where the information on the flare was missing and was not to be found from helioviewer.org. Full table with data from Raukunen et al. [38] as well as our results are in Appendix A.

For each event a value for the solar wind speed was found by averaging values from databases, see appendix A, for $\pm 3\,\mathrm{h}$ from the start of the SEP event. This value can be used to calculate the longitude on the source surface where, based on Parker spiral the Earth is magnetically connected to the Sun. Calculations leading to the following formula are presented, e.g., by Owens et al. [40].

$$\Phi_{\mathrm{Parker}} = \frac{\Omega_{\odot} \cdot (R_{\mathrm{Earth}} - R_{\mathrm{ss}}) \cdot \cos \Theta_{\mathrm{Earth}}}{v_{\mathrm{sw}}} \tag{1}$$

where $\Omega_{\odot}$ is the Sun's rotational speed, R_{Earth} Earths distance from the Sun, R_{ss} is the height of the source surface, Θ_{Earth} the latitude of Earth in Heliocentric Earth Equatorial (HEEQ) coordinate system (following the notation of Thompson [41]) and v_{sw} is the solar wind speed at the starting time of the SEP event. SSW PFSS package uses HEEQ coordinate system.

For the table in Appendix A we additionally traced the magnetic field, using PFSS package provided by SSW, starting from the flare region (defined here as a circular area, around the actual flare location on the solar surface, with radius

$D = 10°$ or when no open field lines were found we tried also $D = 15°$) and calculated the the angular distances of the end points of the open field lines in comparison to the flare site (α in figure 6). The formula for the angular distance is:

$$\alpha = \arccos(\cos\Theta_{\text{flare}} \cos\Theta_{\text{field line}} \cos(\Phi_{\text{field line}} - \Phi_{\text{flare}}) + \sin\Theta_{\text{flare}} \sin\Theta_{\text{field line}}) \quad (2)$$

where Θ_{flare} and Φ_{flare} are the latitude and longitude of the flare site and $\Theta_{\text{fieldline}}$ and $\Phi_{\text{fieldline}}$ the latitude and longitude of the end of the field line.

This angular distance will give us an idea of how far from the Parker longitude can a flare site be while it is still magnetically connected to Earth. Additionally we traced the field down from a circular area on the source surface ($D = 10°$) around the Parker connection point to see how close to the flare site the roots of the field lines might fall, angular distance between the flare site and the closest root of a field line is marked by β in figure 6. This can be used as a secondary measure of connectivity alongside with λ indicated in figure 6, these values are also listed in the appendix A. The angular range around the flare site and the nominal root of the field line is designed to mimic the uncertainties in the interplanetary magnetic field. As the synoptic maps are updated every 6 hours, we used primarily the one available before the onset of the flare and and only when no open field lines were found we used the map from after the flare onset. Hence the magnetic field configuration we consider is pre-existing rather than, e.g., evolving due to the CME.

3.2 Statistical methods

Here we will present the statistical tools, that will be used in chapter 4 to study the correlations and connections between the SEP, flare and CME parameters. We will discuss here the Pearson correlation coefficient (section 3.2.1), Spearman rank-order correlation (3.2.2), Tukey's fast and compact test (3.2.3), Mann-Whitney U-test (3.2.4), Kolmogorov-Smirnov test (3.2.5) and the significance levels (3.2.6).

3.2.1 Pearson correlation coefficient

As described in the Numerical recipes [42], the Pearson product-moment correlation coefficient gives an estimate of the linear dependence between two data sets, described by values from -1 to 1. Values closer to 1 and -1 show correlation, with positive and negative slope respectively. Values closer to zero indicate either lack of correlation or that the correlation is more sophisticated than linear, i.e., cyclic, exponential, etc., or that one of the variables is not normally distributed. Here is the formula for the correlation coefficient:

$$r = \frac{\sum_{i=1}^{n}(x_i - \overline{x})(y_i - \overline{y})}{\sqrt{\sum_{i=1}^{n}(x_i - \overline{x})^2 \sum_{i=1}^{n}(y_i - \overline{y})^2}} \tag{3}$$

Significance of this value can be estimated by calculating a statistic t:

$$t = r\sqrt{\frac{N-2}{1-r^2}}, \tag{4}$$

where N is the size of the sample. In the case of no correlation this t is distributed as a Student's t-distribution with $N-2$ degrees of freedom. Hypothesis is that the correlation is zero, and the significance level of t it is the probability that the hypothesis is correct and there is no correlation.

3.2.2 Spearman rank-order correlation

Aforementioned Pearson correlation coefficient tests linear correlation and Spearman rank-order correlation coefficient is essentially the same, but done after replacing the actual values by their rank among all the values. This method is more robust, but can detect correlation even if the data is nonlinear, as long as it is monotonic. Its significance can be tested the same way as Pearson correlation coefficients. This method is also described in the Numerical recipes [42].

3.2.3 Tukey's fast and compact test

As described by Tukey [43], two unpaired samples can be compared if one of the populations has the smallest value of the both and the other one the largest value of the both. Say the first has the largest value, count how many values are there in the first sample that are larger than the largest value of the second group, call this value a. Next count how many of the values in the second sample are smaller than the smallest value in the first sample, call this value b. Sum up $a + b$, this the total count, which when it is 6, 7, 10 or 13 corresponds to a two-sided significance level 0.10, 0.05, 0.01 and 0.001, which corresponds to the probability of the two samples do not differ from each other.

3.2.4 Mann-Whitney U-test

Richard Lowry [44] describes Mann-Whitney U-test as a non-parametric alternative for t-test, which allows us to compare two samples without assuming that the measurement is done on an equal interval scale or that the source populations would be normally distributed.

The method is as follows: combine the two populations ($n_A + n_B = N$) and rank them, use tied ranks where necessary. Calculate the sums of the ranks of each population separately and combined: T_A, T_B and T_{AB}. The mean rank of combined population is now: $(N + 1)/2$, hence the expected rank sums are: $\mu_{T_A} = n_A(N + 1)/2$, and equivalently for B. The standard deviations of the two sampling distributions can be shown to be the same, i.e., $\sigma = \sqrt{n_A n_B (N + 1)/12}$. When n_A and n_B are larger or equal to 5 the sampling distributions of T_A and T_B approach normal distribution. Therefore they can be transformed into a z-ratio, which can then be referred to a unit normal distribution. The z-ratio formula must include a correction for continuity, -0.5 if $T > \mu_T$ and $+0.5$ if $T < \mu_T$, so it becomes: $z_A = (T_A - \mu_{T_A} \pm 0.5)/\sigma$, and equivalently for population B. The z_A and z_B always

have the same absolute value, but opposite sign so it does not matter which is used for finding the statistical significance. The null hypothesis is that the two sampling distributions have the same mean.

3.2.5 Kolmogorov-Smirnov test

The K-S test, e.g., [42] compares the cumulative distributions the samples were drawn from. The K-S statistic is the maximum value of the absolute value of difference between the two distribution functions:

$$D = \max_{-\infty<x<+\infty} |S_{N_1}(x) - S_{N_2}(x)|. \tag{5}$$

This makes the test more sensitive to differences at the tails of the distribution functions, around the smallest and largest values, as opposed to Mann-Whitney U-test (described above in section 3.2.4) which compares the means of the two populations.

The null hypothesis of the K-S test is that both of the samples are drawn from the same distribution. In this case the distribution of the K-S statistic and a p-value of the observed K-S statistic can be calculated. And finally the p-value can be considered as a significance level for the obtained result.

3.2.6 Significance levels

Significance level corresponds to the probability of a mere chance causing the obtained result. As none of our tests assume one sample to have larger values than the other we must consider a two-sided significance, as presented in figure 7, where test statistic has the value 1.96, which corresponds to 0.05 significance level. If the significance level is small, the null hypothesis is false for the data set in question. In this work we consider significance level 0.05 to be significant and 0.10 almost significant, by which we mean that we consider this level of significance to warrant

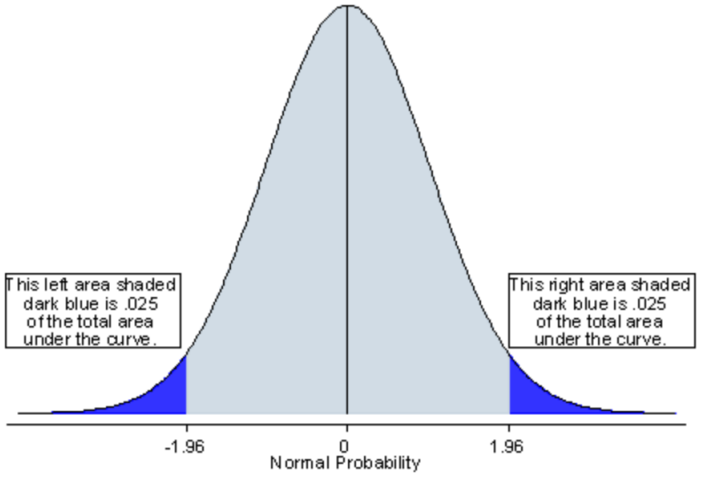

Figure 7. Two sided significance level 0.05, picture from [45].

further investigations while not showing a positive result in our sample. [45]

4 Results

4.1 Magnetic spreading

Wiedenbeck et al. [46] studied the magnetic field expansion in the corona by studying PFSS models from each day from 1998 until 2011. They traced field lines from the equatorial plane back to the solar surface. Whenever they found a large number of field lines rooting to the same region, within a radius R from each other on the solar surface, they considered that as a group of field lines. For each group they measured the longitudinal width of the origin points on the source surface. Finally they chose the largest longitudinal width on each day to be considered as the magnetic spreading that day. These daily magnetic spreadings were plotted as a conjugate cumulative distribution function, reproduced as the blue plots in figure 8. These images compare the longitudinal widths of our events to the results from Wiedenbeck.

In figure 8 are plots of the data from Wiedenbeck et al. [46], and the longitudinal

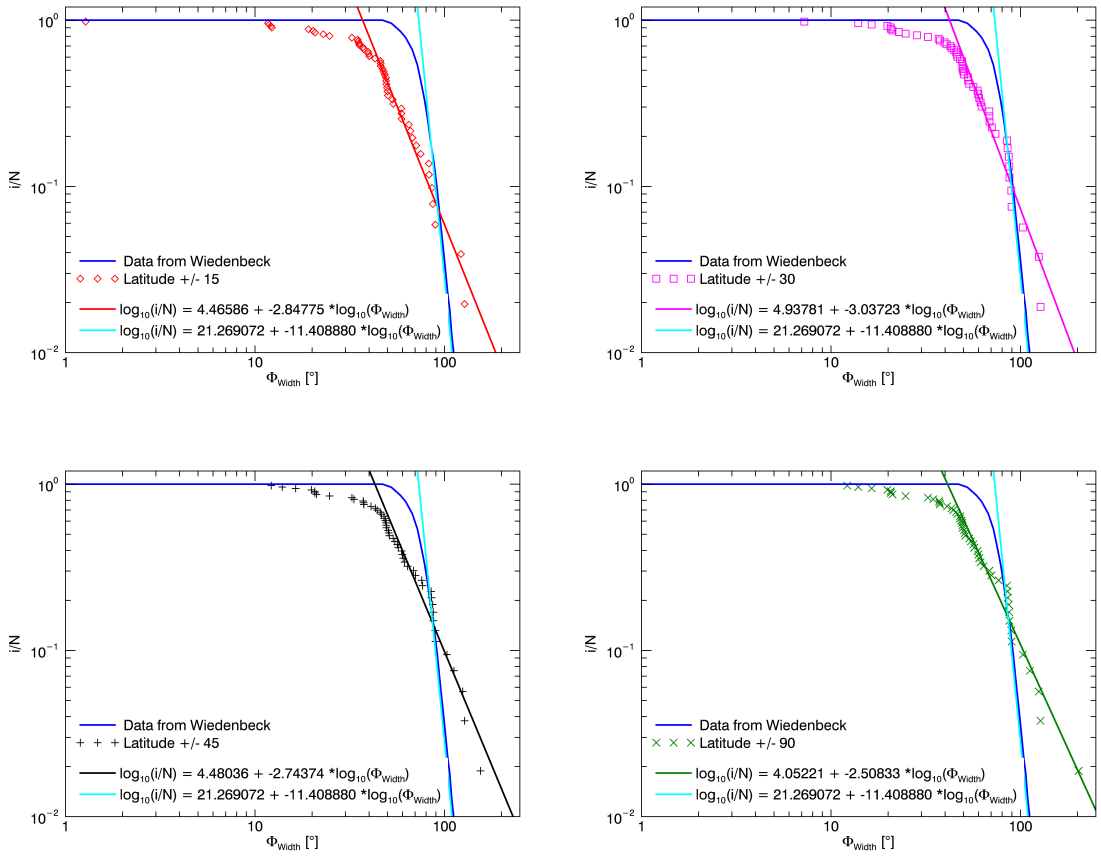

Figure 8. Blue line is a plot reproduced from a graph in a paper by Wiedenbeck et al. [46] showing the magnetic spreading from a region with a radius of $R = 10°$. The other data set is showing the longitudinal width of the magnetic field lines on the source surface at the times of the events in our study, when the PFSS model was traced up from a circle ($D = 10°$) around the flare, with different longitude bands considered. In upper left figure only field lines ending up at latitudes $\pm 15°$ from the equator were considered, whereas on the bottom right all latitudes were taken into consideration. Additionally there are power law functions fitted to each data set excluding points with $i/N \geq 0.5$.

widths of our events when considering different latitude bands: $\pm 15°$, $\pm 30°$,$\pm 45°$, $\pm 90°$. As the events in our data set had some field lines reaching out to very high latitudes near the poles, the data points in the lower left plot in figure 8 are not well comparable to the data from Wiedenbeck. To make the comparison between our events and data from Wiedenbeck more reasonable we neglected field lines reaching outside the aforementioned latitude bands. This did not change the appearance of

Table 1. Some longitudinal widths calculated from the fits in figure 8 at different significance levels.

Fit	Longitudinal width Φ_{Width} [°]			
	$i/N = 0.50$	$i/N = 0.10$	$i/N = 0.05$	$i/N = 0.01$
±15°	47	83	106	186
±30°	53	90	113	192
±45°	55	99	128	230
±90°	54	103	136	259
Wiedenbeck	78	90	95	110

the data points dramatically.

On the y-axis i/N correspond to probability, i is the rank of the event when organized according to the longitudinal width and N is the total number of events. We have excluded events from our data set where there were fewer than ten field lines originating from a circular area with $D = 10°$ around the flare site.

The data sets in figure 8 are fitted with power law functions, particularly to the points $i/N \leq 0.5$. Obtained functions are presented on the plots, the slope of the function for data from Wiedenbeck is -11.4, whereas for our data it is between -2.5 and -3.0. In table 1 are some values calculated from the functions fitted on the plots in figure 8: the longitudinal width for each fit at different significance levels. As we only have so few measurements the last value on the right in the table, 0.01 significance level, is an extrapolation, from beyond our dataset.

4.2 Connectivity

For 60, of the 72 events we used from our data set, it was possible to find ≥ 10 open field lines starting from near ($10° - 15°$ angular distance) the flare site. These events will be used in our study. Nitta et al. [37] found open field lines within 10° from the flaring region in 80 % of their events, for our data set the corresponding value is 75 %.

In figure 9 are the λ connectivity values with an exponential fit to values with $i/N \geq 0.10$. In 49% of the events the closest field line ended up within 10° from

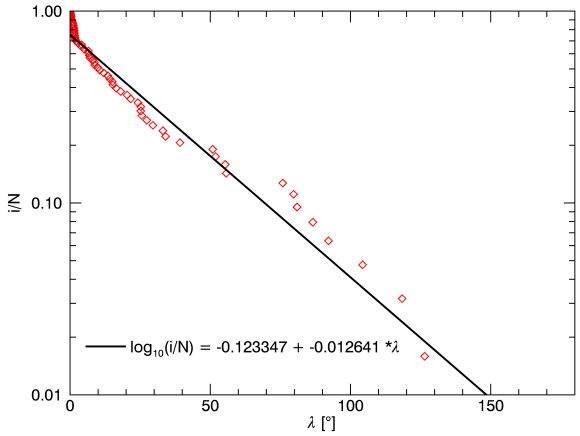

Figure 9. Connectivity values with exponential fit to values with $i/N \geq 0.10$

Table 2. Connectivity values for the given percentages of events when considering the data points in figures 9 (λ), 10 (angular distance between flare site and nominal Parker spiral), and 11 (β).

figure	10 %	25 %	50 %	75 %
9	0.7°	1.6°	11°	33°
10	16°	20°	32°	60°
11	2.0°	5.5°	25°	44°

the nominal Parker spiral connection point. Additionally we considered what was the maximum connectivity within 10 %, 25 %, 50 %, and 75 % of the best connected events, results are in table 2.

In figure 10 are the angular distances between the flare site and the nominal Parker spiral. Similar to figure 9 there is an exponential fit to values with $i/N \geq 0.10$, and some angular distances based on the data points are listed in table 2. The connectivity is maximum 10° only in 3% of the events.

In figure 11 are, in red diamonds, the angular distances between the flare site and the closest magnetic field line root point when the field was traced down from near the Parker spiral connection point, i.e., β connectivity values. The black line is an exponential function fitted to values above $i/N = 0.1$. The closest field line

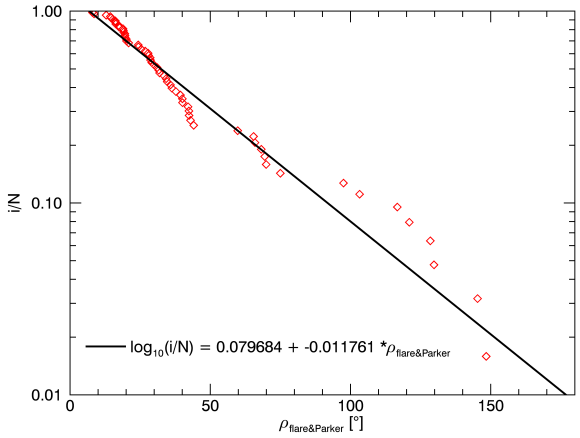

Figure 10. Angular distances between the flare site and nominal Parker spiral with exponential fit to values with $i/N \geq 0.10$

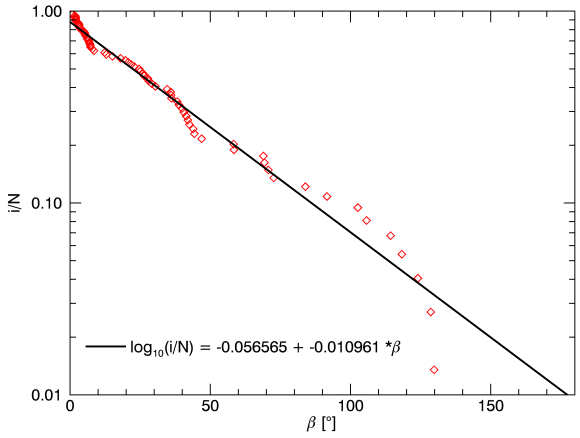

Figure 11. Angular distance between the flare site and the root of the closest magnetic field line. With exponential fit to values with $i/N \geq 0.10$

ended up within 10° from the flare site in 38 % of the events. Maximum connectivity values for some percentiles are in table 2.

The fits in figures 9 and 11 do not differ from each other hugely, . We explored the β value for connectivity briefly as well, but we did not find much difference, so we will not present those results here. We will consider λ as the connectivity from here on.

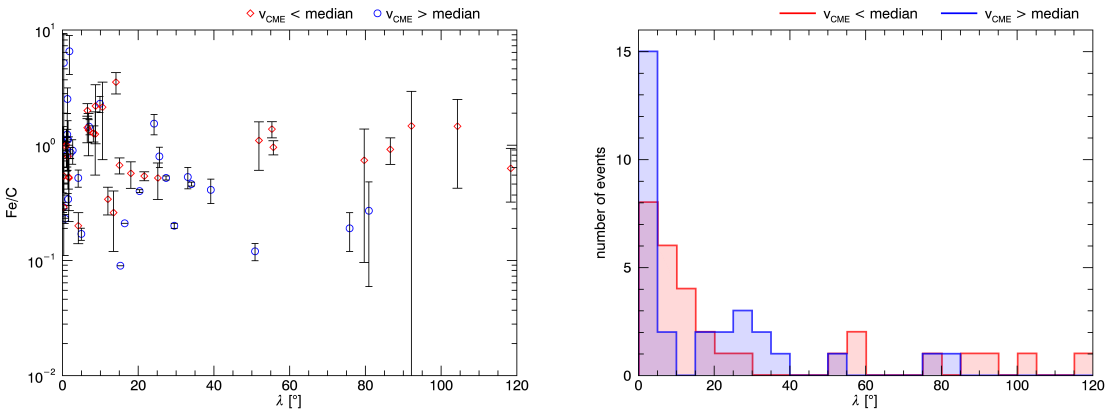

Figure 12. Fe/C ratio plotted against connectivity and a histogram of the values with binsize 5°.

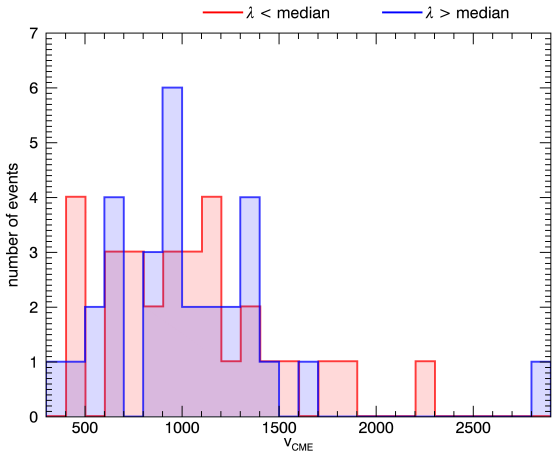

Figure 13. Histogram of the events devided in two by median connectivity (λ) as function of v_{CME}, bin size $100\,\mathrm{km\,s^{-1}}$.

4.3 Connectivity vs. SEP and CME parameters

Next we will look into the connectivity as a function of Fe/C ratio see figures 12 and 13. The events in these plots are devided in two by the median CME speed and the median connectivity, the median values are listed in table 3.

Tukey's fast and compact test, described in chapter 3.2.3, can be considered as a tool here. Looking into the connectivity values in figure 12, we get values which correspond to the significance level of 5 %, see table 4. Tukey's fast and compact

Table 3. Mean values of some quantities in our data set.

Quantity	Mean value
v_{CME}	991 km s^{-1}
Fe/C	0.80
λ	9.3°
dt_{flare}	24 min
I_{flare}	M5.2

Table 4. Results of statistical tests taken in chapters 4.3, 4.4, and 4.5. The tests are described in chapter 3.2. Significance is the two sided significance level obtained from the corresponding test. Significant results are marked with red, almost significant with blue.

Fig.	median	x-axis	Tukey's test			Mann-Whitney U-test		K-S test	
			a	b	significance	z-value	significance	D	significance
12	v_{CME}	λ	4	3	0.05	1.183	0.237	0.233	0.342
13	λ	v_{CME}	1	0	-	0.266	0.790	0.133	0.936
14	Fe/C	λ	1	2	-	-1.469	0.142	0.379	0.022
15	λ	Fe/C	2	2	-	1.626	0.104	0.300	0.109
16	v_{CME}	dt_{flare}	0	2	-	-1.672	0.095	0.345	0.048
17	dt_{flare}	v_{CME}	1	5	0.10	-1.692	0.091	0.340	0.057
18	Fe/C	dt_{flare}	2	3	-	3.144	0.016	0.408	0.012
19	dt_{flare}	Fe/C	2	2	-	2.282	0.022	0.339	0.059
20	dt_{flare}	λ	4	3	0.05	-0.180	0.858	0.286	0.169
21	λ	dt_{flare}	1	1	-	-0.365	0.715	0.207	0.514
22	v_{CME}	I_{flare}	6	0	0.10	-2.519	0.012	0.379	0.022
23	I_{flare}	v_{CME}	1	3	-	-2.578	0.010	0.359	0.033
24	Fe/C	I_{flare}	1	2	-	-0.080	0.936	0.118	0.983
25	I_{flare}	Fe/C	4	0	-	0.781	0.435	0.194	0.586
26	I_{flare}	λ	1	0	-	0.132	0.895	0.138	0.927
27	λ	I_{flare}	1	1	-	0.435	0.663	0.172	0.741

test indicates a difference in the tails of the connectivity distributions of the two populations with fast and slow CME speeds. Looking at the histogram in figure 12 it appears the events with faster CMEs would have a better connection to the flare site in our sample. In figure 13, are the CME speeds of well and poorly connected events, here the difference is not apparent, nor found by taking the Tukey's fast and

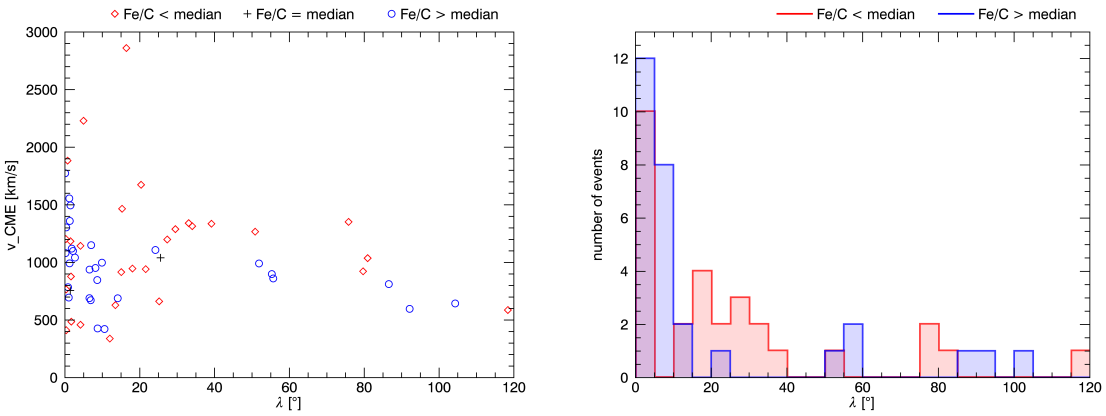

Figure 14. CME speed plotted against connectivity and a histogram of the values with binsize 5°. The events with Fe/C = Fe/C median have been neglected in the histogram.

compact tests, see table 4.

Also the results for the Mann-Whitney U-test and the K-S test on the connectivity values in figures 12 and 13 are listed in table 4. At the significance level of the U-test we can not reject the null hypothesis that the events with slow CMEs have the same median connectivity as the events with fast CMEs or that the well connected events have the same median CME speed than the poorly connected events. Same goes fort the K-S tests, we can not reject the null hypothesis of the K-S test that the cumulative distribution functions of the connectivity values for events with fast and slow CMEs as well as the CME speed for well and poorly connected events are the same. It appears the λ distributions for events with fast and slow CMEs are similar, but there might be differences towards the tails of the distributions.

Next we will look into the connectivity and Fe/C ratio, see figures 14 and 15. The events in these plots are divided in two by the median Fe/C ratio and the median connectivity, the median values are listed in table 3.

For the connectivity values in figures 14 and 15 Tukey's fast and compact test (results in table 4) indicates no difference in connectivity between the samples of high and low Fe/C ratio or in Fe/C ratio between events with good and poor magnetic

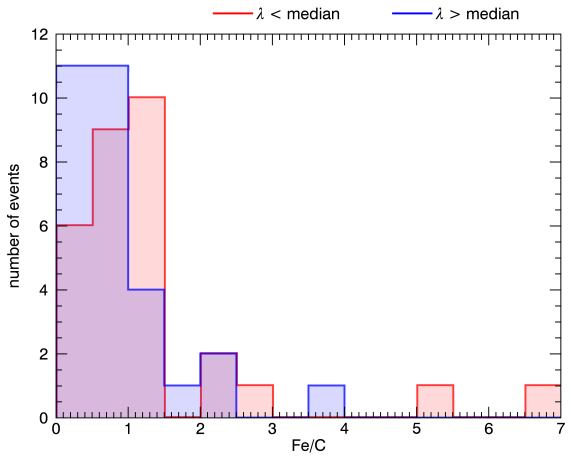

Figure 15. Histogram of the events devided in two by median connectivity (λ). Presented as function of Fe/C, binsize 0.5.

connection.

In table 4 are the results of Mann-Whitney U-test and the K-S test for the connectivity values in figure 14 and 15. We can not reject the null hypothesis of the Mann-Whitney U-test that the median connectivity is the same for high and low Fe/C ratios, nor that the median Fe/C ratio is the same for events with good and poor connectivity. We can, however, reject the null hypothesis of the K-S test taken on the data in figure 14 and say that the cumulative distribution function of the connectivity values of events with low Fe/C ratio is different from the events with high Fe/C ratio, the low Fe/C ratios are more evenly distributed on different connectivity values, when the higher Fe/C ratios are piled up at the better connectivity values. The results of the K-S test on data in figure 15 do not allow us to reject the null hypothesis that the cumulative distributions of Fe/C ratios for the well and poorly connected events are the same.

Hence CME speed appears not to be a factor for the connectivity, but events with large Fe/C ratios appear to be better connected than the events with low Fe/C ratio. Next we will look into the flare parameters and their connection with the Fe/C ratio, CME speed and the connectivity.

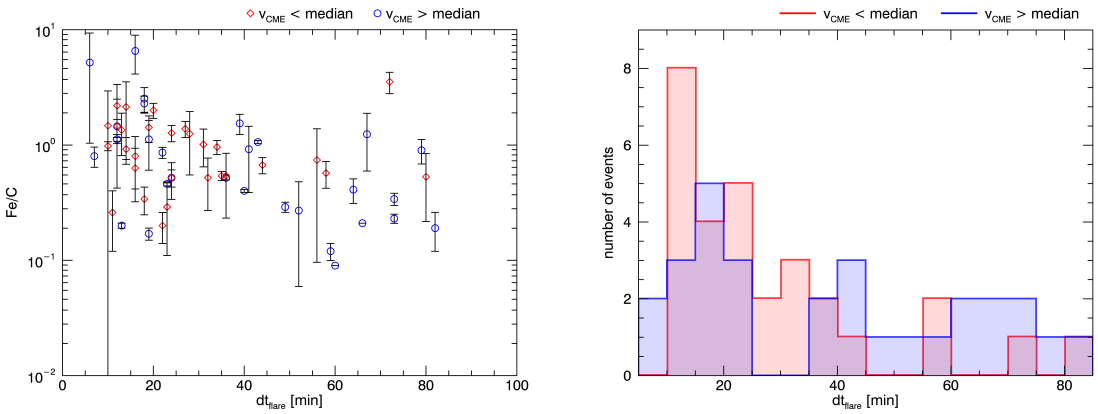

Figure 16. Fe/C ratio plotted against flare duration and the same values in a histogram, bin size 5 min.

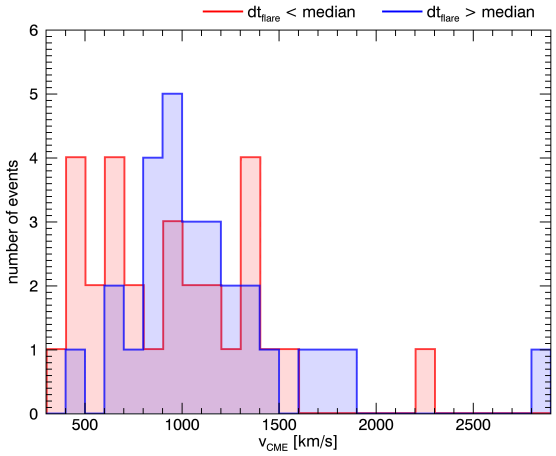

Figure 17. CME speeds of the events divided in groups with short and long duration flares, bin size 100 km s^{-1}.

4.4 Flare duration

In figures 16 and 17 are plotted the flare durations of events with fast and slow CME speed and the CME speeds of short and long flares, mean values in table 3. Flare duration here is simply the difference between the start and end times of the flare as indicated in the table by Raukunen et al. [38].

Tukey's fast and compact test for the flare duration values plotted in figure 16 indicates no difference in the flare duration between events with fast and slow CMEs,

see table 4. The result of the Tukey's fast and compact test on the CME speeds in figure 17 indicates a difference between the short and long flares. Further calculation of Mann-Whitney U-test and K-S test gives values also presented in table 4.

Mann-Whitney U-test indicates difference in the mean flare duration between events with fast and slow CMEs as well as in the mean CME speed between events with short and long flares. K-S test on the CME speeds of events with short and long flares indicates a difference as well and finally KS-test on the flare durations of events with fast and slow CMEs allows us to reject the null hypothesis that the cumulative distributions functions of the flare durations of events with fast and slow CMEs are the same. We will conclude that events with slower CMEs have shorter flares than events with fast CMEs.

In order to compare with the findings of Reames et al. [47] we calculate the Spearman rank-order correlation (described in section 3.2.2) for all the data points in figure 16. This gives as the correlation coefficient -0.222, which corresponds to a significance level of: 0.059. Hence we have found an almost significant correlation between Fe/C ratios and flare duration.

In figures 18 and 19 are the flare durations of the events with high and low Fe/C ratios and the Fe/C ratios of the events with short and long flares, mean values in table 3. Tukey's fast and compact test indicates no differences, see table 4.

Results of Mann-Whitney U-test and the K-S test on the data in figures 18 and 19 are presented in table 4. Mann-Whitney U-test allows us to reject the null hypothesis that the events with low and high Fe/C ratios would have the same mean flare duration or the events with short and long flares would have the same Fe/C ratio. Also results of the KS-test allow us to reject the null hypothesis that the cumulative distribution functions of flare durations in events with low and high Fe/C ratios would be the same. the K-S test on the Fe/C ratios of events with short and long flares gives also an indication of difference. Events with high Fe/C ratio

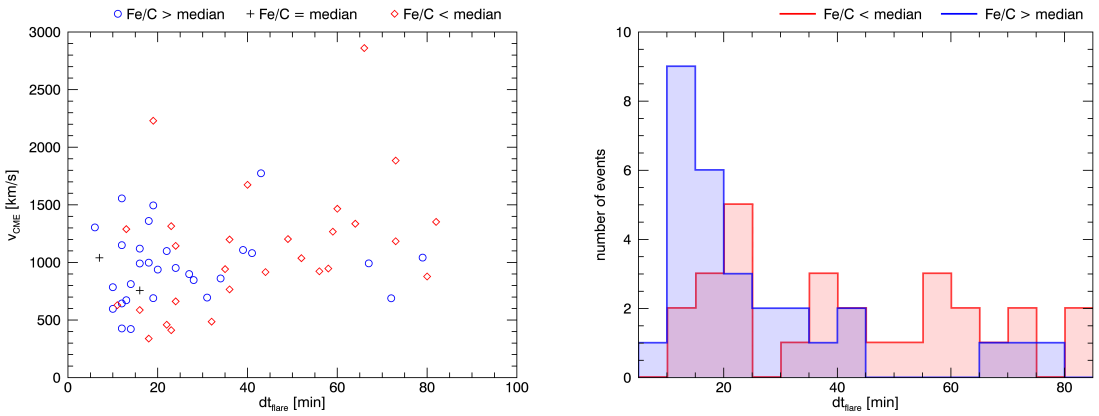

Figure 18. CME speed plotted against the flare duration and the same values in a histogram, bin size 5 min.

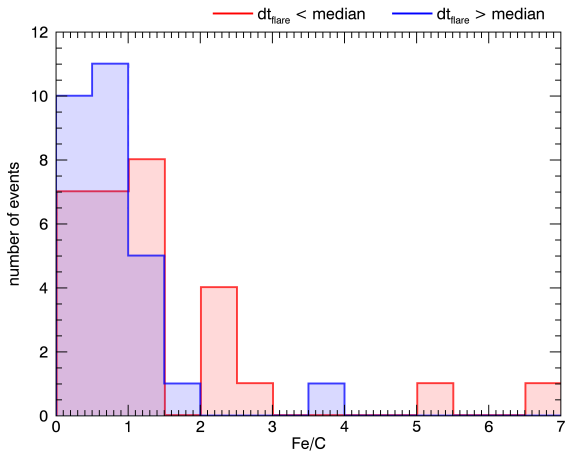

Figure 19. Fe/C ratios of the events divided in groups with short and long duration flares, bin size 0.5.

are clearly associated with shorter flare duration and low Fe/C ratio with longer flare duration.

In figures 20 and 21 are the connectivity values of events with short and long flares and the flare durations of the events with good and poor connectivity, mean values in table 3. The results of the statistical tests taken on these data sets are given in table 4. For the connectivity values of events with short and long flares Tukey's fast and compact test indicates difference in the very tails of the distribution. This

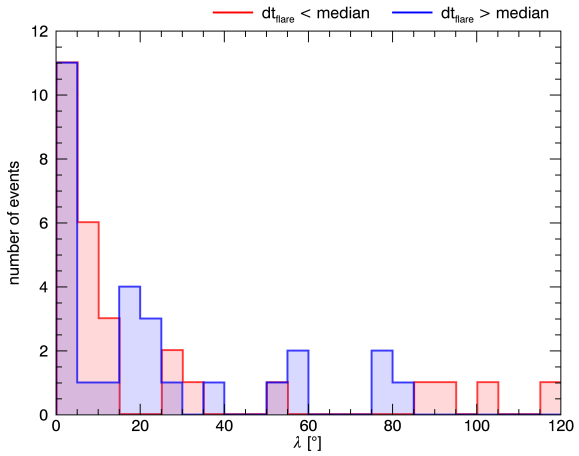

Figure 20. Connectivity of events with short and long flares. Bin size: 5°.

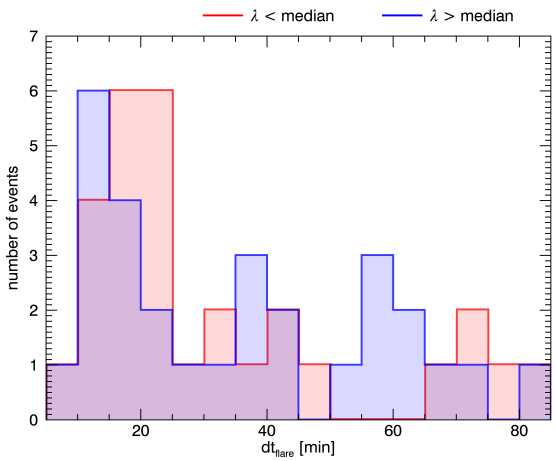

Figure 21. Flare duration of events with good and poor connectivity. Bin size: 5 min.

result is not supported by the other tests, however.

The flare duration appears to be associated with Fe/C ratio and the CME speed, but not strongly with the connectivity λ.

4.5 Flare class

In figures 22 and 23 are plotted the flare class of events with fast and slow CME speed and CME speeds of events with high and low X-ray intensity. The mean

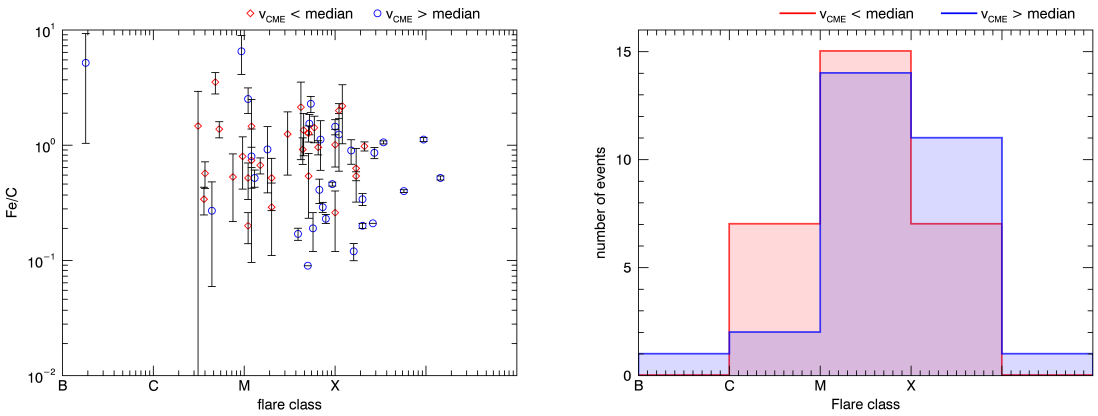

Figure 22. Fe/C ratio plotted against the flare class. Bin size is one order of magnitude in the maximum X-ray intensity.

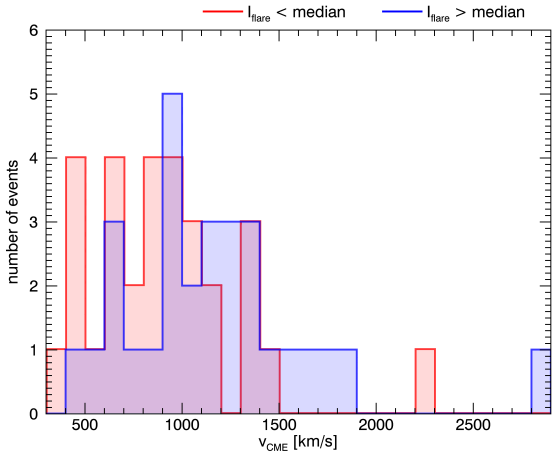

Figure 23. Events divided in two, by flare class, presented as a histogram of CME speeds. Bin size 100 km s^{-1}

values are listed in table 3.

Tukey's fast and compact test, results in table 4, for the flare class data plotted in figure 22 indicates a difference between the populations of more and less intensive flares. For the CME speeds in events with high and low X-ray intensity Tukey's fast and compact test does not show a difference. Further calculation of Mann-Whitney U-test allows us to reject the null hypothesis that the samples of fast and slow CME speeds have the same mean flare class and the samples of events with high and low

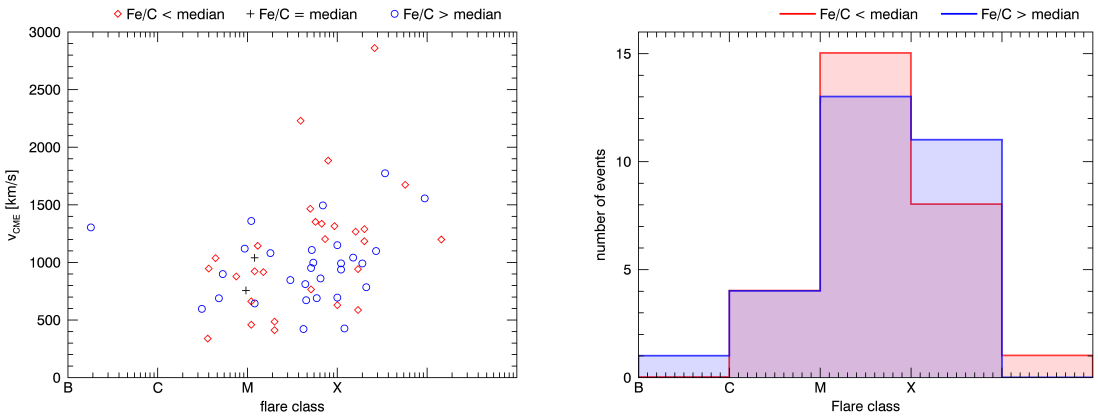

Figure 24. CME speed plotted against the flare class with a histogram presentation. Bin size is one order of magnitude in the maximum X-ray intensity.

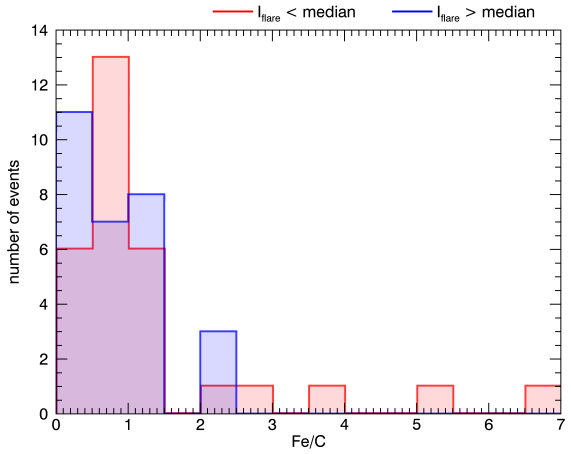

Figure 25. Events divided in two, by flare class, presented as a histogram of Fe/C ratios. Bin size: 0.5.

X-ray intensity have the same mean. The K-S test also allows us to reject the null hypothesis that the cumulative distributions functions are the same. Clearly faster CMEs are associated with stronger flares.

In figures 24 and 25 are plotted the flare class of events with high and low Fe/C ratio and Fe/C ratios of events with high and low X-ray intensity, mean values in table 3. None of the statistical tests taken, see table 4, show a difference between the flare classes of events with high and low Fe/C ratios or Fe/C ratios of events with high and low flare X-ray intensity. There is no difference of flare classes between the

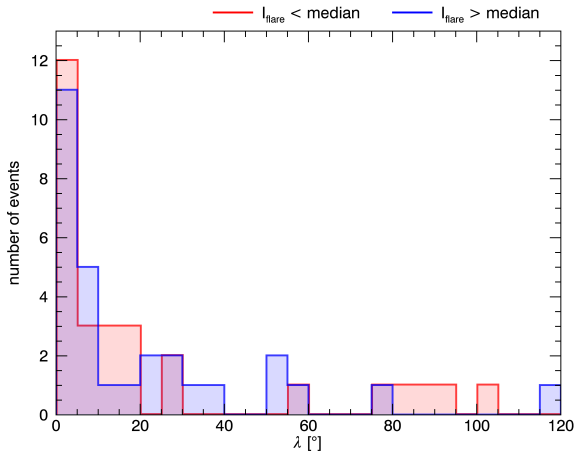

Figure 26. The connectivity of the events with high and low X-ray intensities.

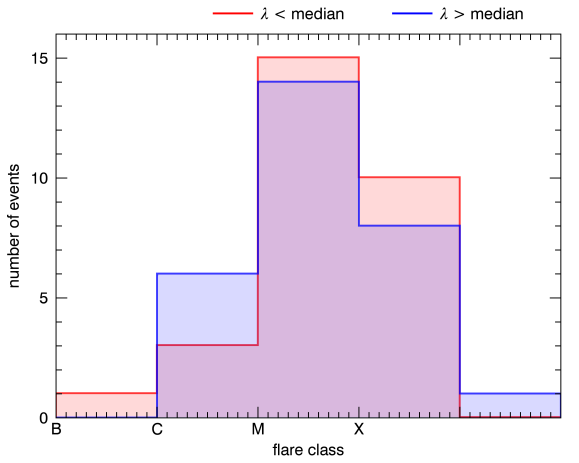

Figure 27. The flare class of the events with good and poor magnetic connection.

high and low Fe/C events in our sample.

in figures 26 and 27 are the connectivity values and the flare classes of the events with strong and weak flares, and good and poor connectivities, respectively. The mean values are listed in table 3. The results of the statistical tests taken on these data sets are presented in tables 4 and indicate no connection between the connectivity and flare class. Also Fe/C ratio is not connected to the flare class in our sample of events, but CME speed clearly is.

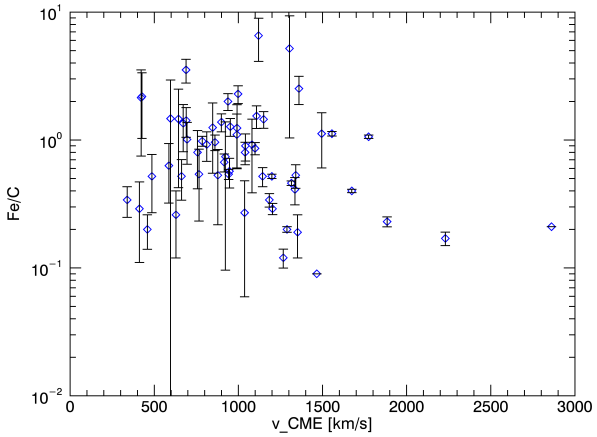

Figure 28. Fe/C ratio with error bars plotted against the CME speed.

4.6 Fe/C ratio and CME speed

Finally lets look at figure 28 and the Fe/C ratios of each event as the function of the CME speed. The Pearson correlation coefficient (described in section 3.2.1) is $r = -0.14$. The significance of this value can be tested by calculating a t-statistic, we get $t = -1.112$, which gives the significance level: 0.271. This value does not allow us to reject the null hypothesis of no linear correlation. We can also calculate the Spearman rank-order correlation coefficient as described in section 3.2.2, which gives us $r_s = -0.24$ with the significance level: 0.059. This value does not either allow us to reject the null hypothesis that there is no correlation between Fe/C ratio and CME speed. However, we consider this almost significant. Thus, there seems to be a weak non-linear anti-correlation between the CME speed and Fe/C ratio.

4.7 Summary of the results

To summarize the results we recall that the magnetic spreading in our data set was wider than found in a previous study [46].

CME speed appears not to be a factor in connectivity, but events with large Fe/C ratios appear to be better connected than events with low Fe/C ratios. 49 %

of the events can be considered well connected as the closest field line ended up within 10° radius from the nominal Parker spiral.

Shorter flares can be associated with higher Fe/C ratios and slower CMEs, whereas longer flares go with lower Fe/C ratios and faster CMEs. Flare duration did not have a clear connection with magnetic connectivity. The flare class seems to not effect the Fe/C ratio or the connectivity, but stronger flares appear with faster CMEs and weaker flares with slower CMEs.

We found also a weak non-linear anti-correlation between the CME speed and Fe/C ratio.

5 Discussion

5.1 Magnetic spreading

The magnetic spreading seems to be a factor in the magnetic connectivity between a flare and Earth. In the observations it appears that the same SEP event can be observed by spacecraft with a huge longitudinal distance [46]. There are also events, such as events number 52 (2003-10-22 17:40) or 13 (2000-03-08 01:31) in our data set, in which the flare and a slow non-halo CME are located on the eastern side of the solar disk, but still an SEP event is seen near Earth.

Looking at the plots in figure 8 we can see that Wiedenbeck et al. [46] have found significant spreading by just looking at daily PFSS models without considering any solar activity underneath. Our data has a quite different approach as it is based on a list of SEP events with information of a flare, which can be assumed to be a source of the SEPs.

The very last point in the plots in the figure 8, is event 73 (2011-11-03 23:39). Here some of the PFSS modeled field lines end up to high latitudes, see figure 29, so it is not directly comparable to the results by Wiedenbeck et al. [46], which is

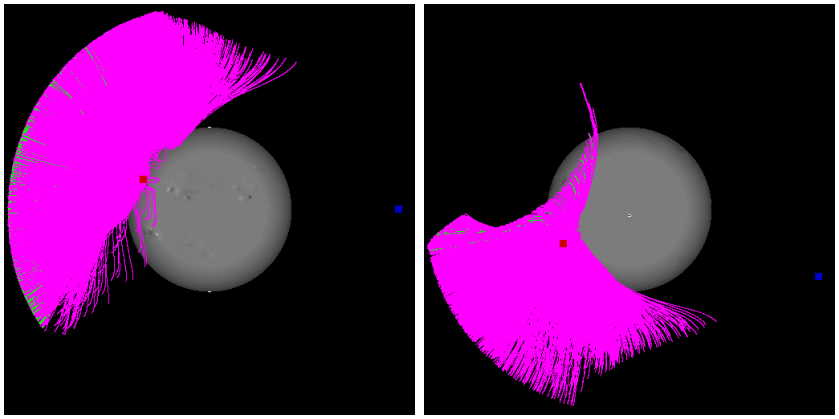

Figure 29. The PFSS plots for event 73. On the right the view from Earth and on the left from solar north. These are the open field lines traced within a 10° radius from the flare site N22E63, indicated by the red square. The blue square indicates the root of the Parker spiral on the source surface, connected to Earth at the time.

why we made several plots with different latitude bands. The distance between the flare site and the farthest field line ($\Delta\phi$) for this event is, however, 82°, so it is the event with the most widely spread magnetic field in our data set.

Looking at values in table 1 it appears that the smaller the latitude band we consider, the better our observations fit under the data points from Wiedenbeck et. al. [46] as the crossing point of the fitted lines falls towards smaller probabilities. However, it is significant that our slopes are much more gradual and hence the probability of finding the more extreme, e.g., $> 100°$ longitudinal width is significantly larger.

As the longitudinal width does not always describe well how far from the flare site the furthest field lines reach out to, we wanted to present also a plot with the α values, see figure 31. In this plot are presented (in red) the largest angular distances between the flare site and the end point of the field line for each event, α is defined in figure 6. First we will, however, discuss shortly individual events. In figure 30 are the field lines of events 17 and 43 on our list, see appendix A, organized by the angular distance between the flare site and the end point of the field line on the source surface.

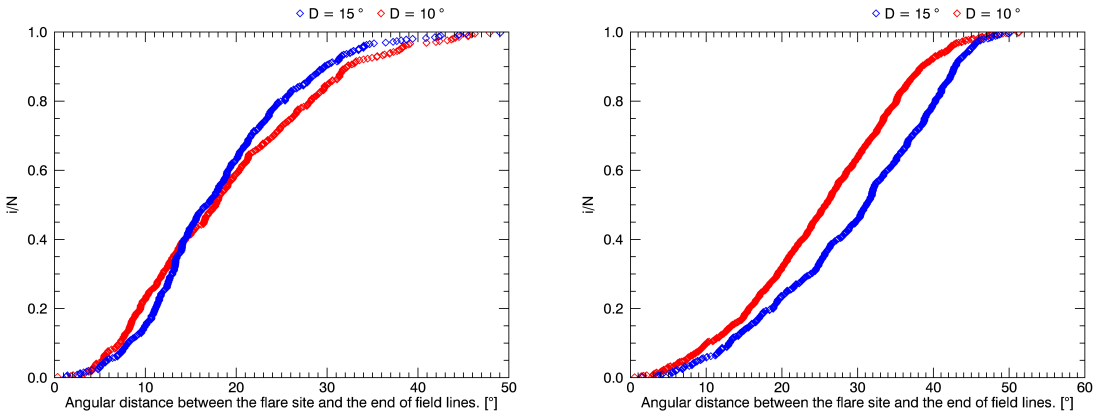

Figure 30. The longitudinal distance between the flare site and each field line for events 17 and 43 on our list, when the radius of the source region is $D = 10°$ (red) and $D = 15°$ (blue).

It was not always possible to find more than ten field lines from a circular area of 10° around the flare site, so for those events the source region has the radius of 15°. We will present the plots in figure 30 to show that changing the radius of the circle from 10° to 15° does not automatically make the magnetic spreading of the event significantly wider. The α, largest angular distance between the flare site and end of a field line, varied $< 1.5°$ with the change in the radius of the source area on the solar surface.

As it is not possible to trace a given number of open field lines from a defined region on the solar surface with SSW's PFSS package, there is different amount of field lines considered for each event. The varying number of field lines traced for each event makes the very last point a little bit arbitrary, see figure 30. This is why we considered additionally the smallest value within the top decile of the angular distances for each event. At the level of this top decile the change of the source region size from $D = 10°$ to $D = 15°$ caused a difference of $-2.5°$ for event 17 and 4.4° for event 43. The change in the size of the source region does not necessarily extend the magnetic spreading, so we expect this change to rather add some scatter than a systematic error into our results. Also if we only considered $D = 10°$ we

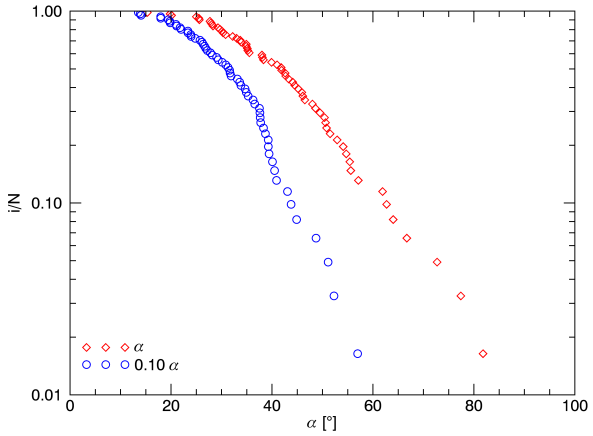

Figure 31. The largest angular distance between the flare site and end of a magnetic field line (α, see figure 6) for each event in red diamonds. In addition top decile in blue.

would be forced to neglect eight more events from our data set.

In figure 31 are the α values and the smallest value in the top decile of the field lines for each event. It seems there is a 10 % chance for the furthest magnetic field to reach over 60° away from the flare site, which would correspond to longitudinal width of 120°, if we assume the field symmetric. This would be even bolder estimation than the values obtained from our fits listed in table 1. This is also wider than what Wiedenbeck et. al. [46] found. The spreading in latitudes and longitudes might differ significantly, however, as even a simple axially symmetric dipole as the boundary condition for PFSS would result latitudinal expansion while longitudinal expansion would be zero.

5.2 Connectivity

The values in table 2 and figures 9, 10, and 11 show well how adding PFSS model to the Parker spiral improves our ability to find magnetic connection.

Based on figure 9 we can say that at least 49 % of the events considered here were well connected. As in that fraction the PFSS model gave a field line going from

within a $10° - 15°$ radius from the flare site to within a $10°$ radius from the Parker connection point. Plots in figure 30 indicate that varying the radius of the source circle does not automatically provide a better connection.

Results from figure 11 can be compared to results of Nitta et al. [37], since they also traced the field lines down from the source surface. We found good connectivity in 38 % of the events in our data set. They had in their data set only impulsive events and they found a good connectivity for 81 % of the events. We go a much better connectivity when we traced the field lines up from the solar surface, so it would be interesting to do that to the events Nitta et al. studied. There are, however, clearly some events where PFSS model can not find open field lines and where the field lines from the PFSS model can not reach the nominal Parker spiral. Also tracing the PFSS model from the nominal Parker spiral would most likely fail in finding the solar source of an SEP event if there was no imaging data. On the other hand the events with better magnetic connection seem to have more qualities that are considered common for impulsive SEP events.

Looking at figures 12 and 13 and the results of the statistical tests in table 4, we found an indication that events with faster CMEs are well connected whereas events with slower CMEs are not. The reason for this result could be the small sample or the fact that the sample contains mainly supposedly flare accelerated events, as generally we would not expect the connectivity matter in the context of a fast wide CME, but the events with slower CMEs should have a connection to the flare site.

Looking at figure 14 and the results of the statistical tests taken in table 4 it appears as events with higher Fe/C ratio seem to have better connectivity, while events with smaller Fe/C ratio are spread more evenly on the plot. Results on the data in figure 15, the Fe/C ratios of well and poorly connected events, call for further investigation, both, the Mann-Whitney U-test and the K-S test almost indicate a difference between the well and poorly connected events. Since we could consider a

good connection to be 10°, as that is the radius of our source region as well, we tried dividing the events as connectivity $> 10°$ and $< 10°$. This way the null hypothesis of the Mann-Whitney U-test can be rejected and even the K-S test indicates difference in the cumulative distributions at almost significant level. Interesting results could also be found by looking into the three events with worse than median connectivity and > 2 Fe/C ratio. From the data available we can, however, conclude that the events with lower Fe/C ratios appear to be less connected than events with high Fe/C ratio. This would point to flare acceleration being more important than acceleration in CME-driven shocks in well-connected than in poorly connected events.

5.3 Flare

Looking at figures 16 and 17 and the results in table 4, faster CMEs are associated with longer flares and slower CMEs with shorter flares. In figures 18 and 19 it appears higher Fe/C ratios are associated with shorter impulsive flares and lower Fe/C ratios with longer flare durations. These results are well in agreement with the idea of dividing SEP events into gradual and impulsive, gradual events the being CME accelerated low Fe/C ratio events and impulsive events having impulsive flares, less significant CMEs and enhancements in Fe/C ratio. Also Reames [47] found that the Fe/O ratio, which is used as a similar measure of the element enhancement as Fe/C ratio, is weakly inversely proportional to the flare duration. Our results agree: the correlation coefficient for the Fe/C ratio as a function of flare duration, see figure 16, is almost significant.

In figures 22 and 24 are the plots of Fe/C ratio and CME speed against flare class. The only B-class flare in these plots is the event 67, it is only B1.8, with a fast CME. There is no big active region on the west limb of the disk or observations of other strong flares and the error bars in the figure 22 are large, which suggest a small SEP event. As the Fe/C ratio could as well be fairly low, and there is observation

of a fast CME around the time we might suspect that it is a CME accelerated event despite the Fe/C ratio.

Looking at the figures 22 and 23 it appears that the stronger flares appear with faster CMEs, which is no surprise. Also the statistical tests taken agree. Even Tukey's fast and compact test would be in agreement if we would neglect the lonely B-class flare event. We would get total count 9, which corresponds to < 0.05 significance level. This is a good example of how a simple test sometimes fails.

In figures 24 and 25 there is no apparent difference in the flare class observed with the high and low Fe/C ratios. The statistical tests done agree. This in good agreement with previous studies, seems that flare of any class can be related to particle acceleration.

The connectivity, see figures 20, 21, 26, and 27 and the results of the statistical tests in table 4, is not connected to the flare properties. Hence, since any kind of flare can be well connected and if they are while there is no fast CME to modify the particle populations we will observe an impulsive SEP event.

5.4 Fe/C ratio and CME speed

Looking at figure 28 there appears to be an inverse correlation between the Fe/C ratio and CME speed. In the case of Pearson correlation coefficient lack of correlation is hardly surprising as by just looking at the data one does not expect to find a linear dependence. The Spearman rank-order correlation coefficient gives a more encouraging result, which can be considered almost significant. This correlation indicates the different acceleration mechanisms: lower metallicities originating from higher in the corona are accelerated by the CME shock and higher metallicities originating from the hot plasma in the flare region possibly with a CME with a low particle accelerating efficiency. Indicated inverse correlation between Fe/C ratio and CME speed is in good agreement with previous results.

6 Conclusions and outlook

In this thesis we studied the magnetic connection between solar flares and Earth during SEP events to find out more about the particle acceleration mechanisms.In the outset, we expected to find a good magnetic connection in events that seemed impulsive, i.e., had high Fe/C ratio or slow CME.

We found wider magnetic spreading than in the previous studies indicating that the magnetic connection can be found even at unlikely situation where the flare is on the East side of the central meridian. These huge longitudinal widths are not very common though, so there is not a magnetic connection to be found between a flare and the observer for each SEP event. It would be interesting to see how different events and a larger data set would behave, maybe set of gradual SEP events and another of impulsive.

We found 49% of the events in our data set to be well connected and that the well connected half of the events had a higher Fe/C ratio than the poorly connected half. The CME speed, however, showed no connection with the connectivity. A case study should be done on the three events with poor connectivity, but Fe/C > 2. Maybe the enhancement could be explained by interaction between quasi-perpendicular shock and suprathermal seed particles from a previous flare [30].

The flare parameters did not show much of a connection with the connectivity values, it appears that at the tails of the distributions the longer flares would be associated with better connectivity. The mean connectivity of the events with short and long flares seems to be the same though.

The flare duration and class were strongly connected to CME speed, stronger, longer flares with fast CMEs and shorter weaker ones with slow CMEs. The Fe/C ratios were not connected to the flare class, as found before any class of a flare can produce an SEP event, but the flare duration appeared to be connected with the Fe/C ratio. This should be studied with the actual flare durations and the few

events with high Fe/C ratio and long flare duration could be also looked into as case studies.

References

[1] J. T. Hoeksema, Proc. Int. Astron. Union **5**, 222 (2009).

[2] P. Higgins, Figshare, `https://figshare.com/articles/Schematic_of_the_Solar_Dynamo/102094`, Accessed April 9, 2019.

[3] E. N. Parker, Astrophys. J. **122**, 293 (1955).

[4] D. V. Reames, Space Sci. Rev. **90**, 413 (1999).

[5] R. C. Carrington, Mon. Not. R. Astron. Soc. **20**, 13 (1895).

[6] K.-L. Klein and S. Dalla, Sp. Sience Rev. **212**, 1107 (2017).

[7] P. F. Chen, Living Rev. Sol. Phys. **8**, 1 (2011).

[8] R. Tousey, *Sp. Res. Conf.* (Akademie-Verlag , 1973), No. XIII, pp. 713–730.

[9] O. E. Malandraki and N. B. Crosby, in *Solar Particle Radiation Storms Forecasting and Analysis*, 1 ed., edited by O. E. Malandraki and N. B. Crosby (Springer , 2018), No. 6, pp. 1–26.

[10] S. E. Forbush, Phys. Rev. **70**, 771 (1946).

[11] J. Wild, S. Smerd, and A. Weiss, Annu. Rev. Astron. Astrophys. **1**, 291 (1963).

[12] D. V. Reames, Space Sci. Rev. **175**, 53 (2013).

[13] H. V. Cane, R. E. McGuire, and T. T. von Rosenvinge, Astrophys. J. **301**, 448 (1986).

[14] D. V. Reames, S. W. Kahler, and C. K. Ng, Astrophys. J. **491**, 414 (1997).

[15] N. Gopalswamy *et al.*, Astrophys. J. **674**, 560 (2008).

[16] A. Afanasiev *et al.*, Astron. Astrophys. **614**, 1 (2018).

[17] A. Kouloumvakos *et al.*, Astrophys. J. **876**, 80 (2019).

[18] D. V. Reames, Astrophys. J. **571**, L63 (2002).

[19] M. A. Lee, J. Geophys. Res. **88**, 6109 (1983).

[20] A. Sandroos and R. Vainio, Astron. Astrophys. **455**, 685 (2006).

[21] C. Marque, A. Posner, and K. Klein, Astrophys. J. **642**, 1222 (2006).

[22] H. V. Cane, D. V. Reames, and T. T. von Rosenvinge, J. Geophys. Res. **93**, 9555 (1988).

[23] D. V. Reames, Space Sci. Rev. **214**, 61 (2018).

[24] S. W. Kahler, Astrophys. J. **562**, 558 (2001).

[25] Y. Wang, M. Pick, and G. M. Mason, Astrophys. J. **639**, 495 (2006).

[26] P. A. Sweet, in *Electromagnetic Phenomena in Cosmical Physics*, Vol. 6 of *IAU Symposium*, edited by B. Lehnert (Cambridge University Press , 1958), p. 123.

[27] V. Petrosian, Space Sci. Rev. **173**, 535 (2012).

[28] M. Dierckxsens *et al.*, Solar Physics **290**, 841 (2015).

[29] A. Papaioannou, I. Sandberg, and A. Anastasiadis, J. Sp. Weather Sp. Clim. **6**, 29 (2016).

[30] A. J. Tylka *et al.*, Astrophys. J. **625**, 474 (2005).

[31] M. Stix, in *The Sun*, edited by M. Harwit, R. Kippenhahn, V. Trimble, and J.-P. Zahn (Springer-Verlag Freiburg, 1989), pp. 96–98.

[32] M. Altschuler and G. J. Newkirk, Sol. Phys. **9**, 131 (1969).

[33] C. J. Schrijver and M. L. Derosa, Sol. Phys. **212**, 165 (2003).

[34] Y. Liu *et al.*, Solar Phys **279**, 295 (2012).

[35] E. N. Parker, Astrophys. J. **128**, 664 (1958).

[36] H. Alfvén, Nature **150**, 405 (1942).

[37] N. V. Nitta *et al.*, Astrophys. J. **650**, 438 (2006).

[38] O. Raukunen, E. Valtonen, and R. Vainio, Astron. Astrophys. **589**, A138 (2016).

[39] J. Torsti *et al.*, Sol. Phys. **162**, 505 (1995).

[40] A. Balogh and G. Erdos, Space Sci. Rev. **176**, 177 (2013).

[41] W. T. Thompson, Astron. Astrophys. **449**, 791 (2006).

[42] W. H. Press, S. A. Teukolsky, W. T. Vetterling, and B. P. Flannery, *Numerical recipes The art of Scientific computing*, 3rd ed. (Cambridge University Press New York, 2007).

[43] J. W. Tukey, Technometrics **1**, 31 (1959).

[44] R. Lowry, Concepts and Applications of Inferential Statistics, `http://vassarstats.net/textbook/index.html`, Accessed April 16, 2019.

[45] U. S. C. Group, Introduction to SAS, `https://stats.idre.ucla.edu/other/mult-pkg/faq/general/faq-what-are-the-differences-between-one-tailed-and-two-tailed-tests/`, Accessed, October 15, 2019.

[46] M. E. Wiedenbeck *et al.*, Astrophys. J. **762**, 9 (2013).

[47] D. V. Reames, H. V. Cane, and T. T. von Rosenvinge, Astrophys. J. **357**, 259 (1990).

[48] R. Vainio *et al.*, J. Sp. Weather Sp. Clim. **3**, 1 (2013).

[49] H. V. Cane, I. G. Richardson, and T. T. Von Rosenvinge, J. Geophys. Res. Sp. Phys. **115**, 1 (2010).

[50] K. Huttunen-Heikinmaa, E. Valtonen, and T. Laitinen, Astron. Astrophys. **442**, 673 (2005).

A Appendix: Additional table

Table from Raukunen et al. [38] with additional information for this study. Notes of the original table:

"Notes. [a] Date and time of the proton event onset from the SEPServer catalog (Vainio et al. [48]), unless otherwise indicated. [b] X-ray flare identification from Cane et al. [49] with additional information from NOAA GOES X-ray flare database, unless otherwise indicated. [c] CME information from Cane et al. [49] unless otherwise indicated, except for the width, which for all events is adopted from the SOHO/LASCO CME catalog. A gap in the LASCO observations is marked by "dg". [d] Event-averaged Fe/C ratio. [e] Time of the proton onset determined with the Poisson-CUSUM-method described in Huttunen-Heikinmaa et al. [50], using 12.6–13.8 MeV protons. [f] Proton event onset during a SOHO/ERNE data gap; onset time determined as the first minute after the gap. [g] X-ray flare identified based on information from the NOAA GOES X-ray flare database. [h] CME identified based on information from the SOHO/LASCO CME catalog."

[i] Missing flare data found from Helioviewer. [j] Solar wind speed averaged over ±3 h from the start of the SEP event. Data ACE/SWEPAM, unless otherwise indicated. [k] Parker longitude. [l] In the case of missing SWEPAM data, solar wind speed was found from OMNIweb. [m] Time of the synoptic map used to trace the field lines of PFSS model, before or after start of the flare. [n] Radius of the source region around the flare site. [o] The number of found open field lines and the number of field lines attempted to be traced. [p] The angular distance between the flare site and the furthest field line, see figure 6. [q] Connectivity value, λ, on the source surface, see figure 6. [r] Connectivity value, β, on the solar surface, see figure 6. D for tracing the field lines down from the source surface was always 10°.

Events with missing flare data were left out of our study and here painted grey.

Additional table

ID	SEP event			Flare					CME			Fe/C	Solar wind								
	date	time	Dur. (h)	Start	Max	End	Pos.	Class	Time	Width (deg)	Speed (km s^{-1})		Speed[j] (km s^{-1})	Parker[k] (deg)	before / after[m]	D[n]	open / all[o]	α[p] (deg)	λ[q] (deg)	β[r] (deg)
1	1997-11-07	06:41	54	05:52	05:58	06:02	S14W33	X2.1	06:10	360	785	0.98 ± 0.09	322[l]	75.22	before	10	1 717 / 80 629	77.4	0.8	3.0
2	1997-11-06	12:37	178	11:49	11:55	12:01	S18W63	X9.4	12:10	360	1556	1.12 ± 0.04	349[l]	69.42	before	10	3 037 / 81 664	72.7	1.2	0.7
3	1998-05-02	14:10	90	13:31	13:42	13:51	S15W15	X1.1	14:06	360	938	2.00 ± 0.30	612	39.58	before	10	595 / 80 634	38	6.6	2.0
4	1998-05-06	08:29	68	07:58	08:09	08:20	S11W65	X2.7	08:29	190	1099	0.86 ± 0.09	456	53.14	before	10	630 / 79 996	48.6	2.2	5.5
5	1998-05-09	04:32	128	03:04	03:40	03:55	SXXW100	M7.7	03:35	178	2331	0.52 ± 0.10								
6	1998-05-27	14:48[e]	47	13:30	13:35	14:50	N18W58	C7.5	13:45	268	878	0.53 ± 0.31	353	68.77	before	10	735 / 816 748	35.5	1.6	4.9
7	1998-10-18	22:22	55	-----	-----	-----	NXXW120	-----	dg	dg	dg	0.90 ± 0.40								
8	1998-11-14	06:16	10	-----	-----	-----	NXXW120	-----	dg	dg		1.73 ± 0.24								
9	1999-05-27	11:16	129	11:36	11:43	11:54	S30E78	C4.5	11:06	360	1691	0.42 ± 0.34	456	53.23	before	10	0 / 1 711 303	-	-	91.6
10	1999-06-04	15:46[e]	153	06:52	07:03	07:11	N17W69	M3.9	07:27	150	2230	0.17 ± 0.02	400	60.7	before	10	862 / 81 400	49.5	5.0	3.3
11	1999-12-28	02:58[e]	51	00:39	00:48	00:52	N20W56	M4.5	00:54	82	672	1.35 ± 0.54	449	54.03	before	15	1 051 / 823 438	35.1	6.9	12.3
12	2000–02–18	09:57	103	-----	-----	-----	NXXW120	-----	09:54	118	890	3.70 ± 3.10								
13	2000-03-08	01:31[e]	12	16:01	16:07	16:13	S22E77	M1.2	16:30	108	644	1.46 ± 1.03	437	55.12	before	15	329 / 829 677	51.5	104.3	114.3
14	2000-05-01	11:29[e]	12	10:16	10:27	10:34	N20W54	M1.1	10:54	54	1360	2.52 ± 0.63	435	55.67	before	10	222 / 82 236	41	1.3	7.0
15	2000-05-04	12:40[e]	33	10:57	11:08	11:14	S20W90	M6.8	11:26	170	1404	1.97 ± 1.50	458	52.9	before	10	0 / 822 195	-	-	42.5
16	2000-06-04	13:06[e]	47	06:24	06:30	06:34	N21E45	C3.1	07:31	17	597	1.47 ± 1.47	458	53.01	before	15	341 / 826 698	38.3	92.1	105.7
17	2000-06-10	17:26	124	16:40	17:02	17:19	N22W40	M5.2	17:08	360	1108	1.54 ± 0.31	479	50.69	after	15	32 / 829 651	15.3	24.2	21.8
18	2000-06-15	21:00[e]	33	19:38	19:57	20:19	N20W62	M1.8	20:06	116	1081	0.92 ± 0.53	592	41.01	before	10	3416 / 82 411	62.7	0.2	6.8
19	2000-06-18	02:29	56	01:52	01:59	02:03	N23W85	X1.0	02:10	132	629	0.26 ± 0.14	412	58.92	before	10	5019 / 83 379	46.5	13.5	12.9
20	2000-06-23	15:06[e]	39	14:18	14:31	14:46	N23W72	M3.0	14:54	198	847	1.25 ± 0.70	488	49.72	before	10	969 / 83 277	39.9	8.6	5.2
21	2000-07-11	01:00[e]	82	21:05	21:42	22:27	N18E49	M5.7	21:50	289	1352	0.19 ± 0.07	441	54.92	before	10	721 / 81 481	41.8	75.8	83.9
22	2000-07-14	10:37		10:03	10:24	10:43	N22W07	X5.7	10:54	360	1674	0.40 ± 0.01	586[l]	41.32	before	10	3865 / 83 045	33.9	20.3	19.7
23	2000-08-12	11:25[e]	106	09:45	09:56	10:09	S17W79	M1.1	10:35	168	662	0.52 ± 0.18	604	39.94	before	10	1826 / 81 132	33.7	25.2	36.0
24	2000-09-19	12:08[e]	128	08:06	08:26	08:42	N14W46	M5.1	08:50	76	766	0.54 ± 0.31	639	37.71	before	10	8348 / 80 417	52.9	0.3	6.5
25	2000-10-16	07:39	150	06:40	07:28	09:11	NXXW95	M2.5	07:27	360	1336	1.02 ± 0.14								
26	2000-10-25	12:40	102	08:45	11:25	15:21	SXXW120	C4.0	08:26	360	770	0.50 ± 0.11								
27	2000-10-30	12:47[e]	12	-----	-----	-----	-----	-----	dg	dg	dg	2.21 ± 2.02								
28	2000-11-24	05:43	115	04:55	05:02	05:08	N22W03	X2.0	05:30	360	1289	0.20 ± 0.01	350	69.34	before	10	822 / 82 686	38.1	29.5	69.3
29	2001-01-28	16:58	199	15:40	16:00	16:24	S04W59	M1.5	15:54	360	916	0.67 ± 0.11	318	75.97	after	15	281 / 789 677	30.3	15.1	22.9
30	2001-03-10	07:39[e]	72	04:00	04:05	04:07	N27W42	M6.7	04:26	81	819	0.34 ± 0.22	419	57.49	before	10	0 / 845 184	-	-	24.6
31	2001-03-29	11:49	97	09:57	10:15	10:32	N16W12	X1.7	10:26	360	942	0.54 ± 0.05	536	44.99	before	10	66 / 810 800	20.1	21.6	30.4

Additional table

ID	SEP event			Flare					CME			Fe/C	Solar wind								
	date	time	Dur. (h)	Start	Max	End	Pos.	Class	Time	Width (deg)	Speed (km s^{-1})		Speed (km s^{-1})	Parker (deg)	before / after	D	open / all	α (deg)	λ (deg)	β (deg)
32	2001-04-02	12:24	10	10:58	11:36	12:05	N16W62	X1.1	11:26	80	992	1.24 ± 0.64	555	43.47	before	10	1 333 / 81 162	54.1	1.2	0.2
33	2001-04-12	11:01	63	09:36	10:28	10:49	S19W43	X2.0	10:31	360	1184	0.34 ± 0.04	628	38.47	before	10	19 / 818 822	19.8	1.5	26.4
34	2001-04-15	14:05	61	13:19	13:50	13:55	S20W84	X14.4	14:06	167	1199	0.52 ± 0.02	498	48.53	before	10	406 / 82 335	34.9	27.3	58.3
35	2001-09-11	04:14 [e]	45	00:49	01:11	01:23	-----	M2.6	01:55	78	304	2.33 ± 1.12								
36	2001-10-22	15:51	227	14:27	15:08	15:31	S21E18	M6.7	15:06	360	1336	0.41 ± 0.10	531	45.53	before	10	2790 / 82 443	54.7	39.2	39.9
37	2001-11-04	16:45	304	16:03	16:20	16:57	N06W18	X1.0	16:35	360	1810	0.25 ± 0.01	315	76.89	before	10	0 / 790 038	-	-	1.8
38	2002-01-27	13:38	134	-----	-----	-----	NXXW120	-----	12:30	360	1136	0.80 ± 0.38								
39	2002–Feb–20	05:58	109	05:52	06:12	06:16	N12W72	M5.1	06:30	360	952	1.27 ± 0.20	406	59.36	before	10	100 / 79 971	27.7	8.2	3.6
40	2002-04-14	10:15 [e]	69	07:28	07:39	07:44	N19W57	C9.6	07:50	76	757	0.80 ± 0.38	391	61.79	before	10	1006 / 81 928	44.1	1.4	7.3
41	2002-05-30	06:39 [e]	51	04:24	05:32	06:13	NXXW100	M1.3	05:06	144	1625	1.10 ± 0.84								
42	2002-07-19	07:17 [e]	70	23:08	23:17	23:23	-----	C8.2	01:32	85	654	0.21 ± 0.06								
43	2002-08-03	23:13 [e]	33	18:59	19:07	19:11	S16W76	X1.0	19:32	138	1150	1.45 ± 0.21	437	55.26	before	10	408 / 80 899	46.1	7.0	18.0
44	2002-08-05	07:58 [e]	85	04:21	05:17	05:33	S10W43	C4.8	07:32	43	689	3.53 ± 0.73	432	55.89	after	10	292 / 1 195 555	25	14.1	25.0
45	2002-08-18	22:10	35	21:12	21:25	21:37	S12W19	M2.2	21:54	140	682	4.35 ± 0.42	542	44.48	after	10	5 / 1 200 958	11	25.2	29.1
46	2002-08-20	08:46	42	08:22	08:26	08:30	S10W38	M3.4	08:54	122	1099	7.05 ± 0.50	477	50.54	before	10	0 / 796 648	-	-	27.7
47	2002-08-22	02:30	47	01:47	01:57	02:05	S07W62	M5.4	02:06	360	998	2.29 ± 0.36	414	58.22	before	10	83 / 1 187 123	33	9.9	4.0
48	2002-10-30	04:03 [e]	240	02:53	02:58	03:11	N30W66	C3.6	05:50	100	339	0.34 ± 0.09	480	50.42	before	10	262 / 85 381	25.5	12.0	42.0
49	2003-11-26	19:09 [e]	92	18:26	18:35	18:39	N26W87	C3.6	-----	-----	-----	0.87 ± 0.80	397	61.14	before	10	0 / 842 242	-	-	36.1
50	2003-05-31	02:56	74	02:13	02:24	02:40	S07W65	M9.3	02:30	360	1835	0.34 ± 0.09	762	31.86	before	10	0 / 791 938	-	-	40.5
51	2003-08-19	09:02 [e]	36	07:38	07:59	08:01	S12W64	M2.0	08:30	35	412	0.29 ± 0.18	430	56.07	before	10	1425 / 80 157	29.7	0.3	6.1
52	2003-10-22	17:40 [e]	96	15:57	16:01	16:04	N03E17	M1.2	16:30	23	1040	0.80 ± 0.16	566	42.72	before	10	6427 / 78 516	57.1	25.6	70.7
53	2004-07-22	17:33	71	07:41	07:59	08:08	N04E10	C5.3	08:30	132	899	1.38 ± 0.22	433	55.86	after	10	205 / 78 796	34.9	55.3	46.9
54	2004-10-30	07:58 [e]	7	06:08	06:18	06:22	N13W22	M4.2	06:54	360	422	2.14 ± 1.38	407	59.47	before	10	608 / 80 231	45.2	10.6	38.8
55	2004-10-30	14:43 [e]	3	11:38	11:46	11:50	N13W25	X1.2	12:30	360	427	2.19 ± 1.16	422	57.36	before	10	602 / 80 401	42.6	8.7	35.9
56	2004-10-30	18:01 [e]	36	16:18	16:33	16:37	N13W28	M5.9	16:54	360	690	1.42 ± 0.37	429	56.42	before	10	821 / 80 269	43.3	6.6	2.0
57	2004-11-01	06:15	155	03:04	03:22	03:26	N12W49	M1.1	03:54	192	459	0.20 ± 0.06	422	57.37	before	10	88 / 801 532	28.3	4.2	2.5
58	2005-01-15	23:35	289	22:25	23:02	23:31	N15W05	X2.6	23:07	360	2861	0.21 ± 0.00	536	45.15	before	10	258 / 80 791	27.9	16.4	58.4
59	2005-05-06	02:57 [e]	11	03:05	03:14	03:21	S04W71	C9.3	03:30	109	1120	6.54 ± 2.41	354	68.45	before	10	719 / 78 936	30.8	1.8	2.0
60	2005-05-06	14:06 [e]	70	11:11	11:28	11:35	S04W76	M1.3	11:54	129	1144	0.52 ± 0.09	380	63.77	before	10	664 / 78 992	29.3	4.2	7.9
61	2005-06-16	20:35	134	20:01	20:22	20:42	N09W85	M4.0	dg	dg	dg	0.71 ± 0.29	658	36.89	before	10	0 / 794 800	-	-	26.0
62	2005-08-29	14:28	65	-----	-----	-----	SXXW120	-----	10:54	360	1600	0.31 ± 0.17								

Additional table

ID	SEP event			Flare					CME			Fe/C	Solar wind								
	date	time	Dur. (h)	Start	Max	End	Pos.	Class	Time	Width (deg)	Speed (km s^{-1})		Speed (km s^{-1})	Parker (deg)	before / after	D	open / all	α (deg)	λ (deg)	β (deg)
63	2006-11-21	20:36 [e]	12	-----	-----	-----	SXXW120	-----	dg	dg	dg	2.95 ± 2.55									
64	2006-12-13	02:59	35	02:14	02:40	02:57	S06W23	X3.4	02:54	360	1774	1.06 ± 0.03	657[l]	36.96	before	10	6 195 / 79 130	48	0.1	5.4
65	2006-12-14	23:08	206	21:07	22:15	22:26	S07W46	X1.5	22:30	360	1042	0.90 ± 0.22	858	28.3	before	10	6 048 / 79 174	50.8	2.7	0.5
66	2010-06-12	02:43	68	00:30	00:57	01:02	N23W43	M2.0	01:32	119	486	0.52 ± 0.25	364	66.7	before	10	5201 / 83 223	50.6	1.7	3.2
67	2010-09-01	01:28	23	21:50	21:53	21:56	N26W37[i]	B1.8	21:17	360	1304	5.19 ± 4.16	336[l]	71.7	before	10	6 348 / 84 304	55.4	0.3	3.2
68	2011-03-21	03:27	137	-----	03:09[i]	-----	N16W36[i]	-----	02:24	360	1341	0.53 ± 0.11	352	68.46	before	10	2 980 / 81 171	55.6	33.1	15.1
69	2011-06-05	05:10	50	02:11	02:14	02:17	S21W25[i]	B3.5	03:00	27	573	0.87 ± 0.22	518	46.87	before	10	0 / 824 968	-	-	44.3
70	2011-06-07	07:36	80	06:16	06:41	06:59	S21W54	M2.5	06:49	360	1255	0.60 ± 0.11	396	61.32	before	10	0 / 825 642	-	-	34.6
71	2011-08-04	04:40	110	03:41	03:57	04:04	N19W36	M9.3	04:12	360	1315	0.46 ± 0.02	349	69.2	before	10	23 / 819 268	25.6	34.0	28.0
72	2011-08-09	08:22	122	07:48	08:05	08:08	N17W69	X6.9	08:12	360	1610	0.69 ± 0.15	602	40.09	before	10	0 / 813 681	-	-	41.4
73	2011-11-03	23:39	155	20:16	20:27	20:32	N22E63	X1.9	23:30	360	991	1.10 ± 0.49	343[l]	70.6	before	10	6 496 / 82 945	81.8	51.9	118.3
74	2012-03-13	17:53	173	17:12	17:41	18:25	N19W59	M7.9	17:36	360	1884	0.23 ± 0.02	575[l]	41.9	before	10	3 902 / 82 045	61.9	0.7	7.2
75	2012-07-08	23:59 [f]	89	16:23	16:32	16:42	S14W83	M6.9	16:54	157	1495	1.12 ± 0.52	431	56.22	before	10	944 / 80 873	50.4	1.5	8.5
76	2012-09-28	06:31 [f]	129	23:36	23:57	00:34	N06W37	C3.7	00:12	360	947	0.57 ± 0.15	368[l]	65.51	before	15	124 / 791 580	30.1	18.1	43.9
77	2013-04-11	08:10	106	06:55	07:16	07:29	N09E12	M6.5	07:24	360	861	0.96 ± 0.13	419	57.64	before	10	345 / 794 568	41.9	55.7	72.6
78	2013-05-13	12:56 [e]	40	01:53	02:17	02:32	N11E89	X1.7	02:00	360	1270	1.48 ± 1.21	419	57.87	before	15	2 / 800 593	24.6	126.4	129.8
79	2013-05-22	13:47	227	13:08	13:32	14:08	S18W15	M5.0	13:26	360	1466	0.09 ± 0.00	444	54.66	before	10	895 / 81 615	35.2	15.3	20.7
80	2013-06-28	05:48 [e]	46	01:36	01:59	02:28	S16E14	C4.4	02:00	360	1037	0.27 ± 0.21	402	60.34	before	15	980 / 812 494	64	80.9	38.2
81	2013-10-25	13:49	64	07:53	08:01	08:09	S08E73	X1.7	08:12	360	587	0.63 ± 0.31	330	73.3	after	15	22 / 794 604	28.1	118.4	128.6
82	2013-10-28	06:19	12	01:41	02:03	02:12	N04W66	X1.0	02:24	360	695	1.01 ± 0.36	284	85.2	before	10	1 973 / 78 805	45.9	1.0	2.0
83	2013-10-28	18:49	16	15:07	15:15	15:21	S08E28	M4.4	15:36	360	812	0.92 ± 0.24	272	88.96	before	10	61 / 793 319	32.2	86.6	102.6
84	2014-04-18	13:42	157	12:31	13:03	13:20	S20W34	M7.3	13:26	360	1203	0.29 ± 0.03	450	53.72	before	10	1 088 / 82 214	66.7	0.3	6.1
85	2014-05-07	19:15 [e]	33	16:07	16:29	17:03	N15E50	M1.2	16:24	360	923	0.74 ± 0.64	335	72.17	before	10	318 / 80 691	42.7	79.7	124.0
86	2014-09-10	19:28	104	17:21	17:45	18:20	N14E02	X1.6	18:00	360	1267	0.12 ± 0.02	361	66.72	before	10	860 / 80 698	44.5	50.8	68.9